Nonlinear topology optimization of flexoelectric soft dielectrics at large deformation

Xing Chen, Song Yao, Julien Yvonnet

▶ To cite this version:

Xing Chen, Song Yao, Julien Yvonnet. Nonlinear topology optimization of flexoelectric soft dielectrics at large deformation. Computer Methods in Applied Mechanics and Engineering, 2024, 427, pp.117005. 10.1016/j.cma.2024.117005 . hal-04779906

HAL Id: hal-04779906
https://univ-eiffel.hal.science/hal-04779906v1

Nonlinear topology optimization of flexoelectric soft dielectrics at large deformation

Xing Chen[a,b], Song Yao[a], Julien Yvonnet[b,*]

[a]*Key Laboratory of Traffic Safety on Track, Ministry of Education, School of Traffic & Transportation Engineering,Central South University, Changsha 410075, China*
[b]*Laboratoire Modélisation et Simulation Multi Échelle MSME UMR 8208 CNRS, Université Gustave Eiffel, F-77474 Marne-la-Vallée, France*

Abstract

We propose a novel nonlinear topology optimization framework tailored for flexoelectric soft dielectrics undergoing large deformation. A numerical method based on Isogeometric analysis (IGA) is introduced to nonlinear soft dielectrics at finite strain, ensuring the C^1-continuity for flexoelectric problems. We outline the process of consistent linearizations and IGA discretizations. Additionally, we introduce an innovative and efficient Strain Density Function (SDF) interpolation scheme for optimizing electromechanical coupling factors (ECFs). In this scheme, the interpolation of electromechanical and hyper-elastic energy terms is grounded in the SIMP model, while a linear material interpolation model is employed for the dielectric energy. Our numerical analysis highlights the remarkable performance of the proposed SDF interpolation scheme in nonlinear electromechanical optimization scenarios. An energy remedy scheme is applied to void regions to eliminate the instability of nonlinear optimization, effectively preventing distortion deformations in low-stiffness elements. Furthermore, we investigate the influence of size effect and larger deformation on the optimization of flexoelectric soft materials. The proposed topology optimization framework adeptly leverages the interplay between size effect and larger deformation, resulting in a notable improvement in ECFs within the optimized structures. Finally, the electromechanical coupling factors (ECFs) of the optimized structures in all the examined cases exhibit enhancements up to 9 times as compared to the reference guess designs.

Keywords: Flexoelectricity, Topology optimization, Nonlinear dielectrics, Large

---

[*] Corresponding author
Email address: `julien.yvonnet@univ-paris-est.fr` (Julien Yvonnet)

Preprint submitted to Journal of Elsevier Science *April 18, 2024* deformation, Isogeometric analysis

---

1. Introduction

In recent decades, the pursuit of harvesting energy from ambient mechanical vibrations has gained substantial attention. This trend is particularly significant for micro/nano-electromechanical systems (MEMS/NEMS)[1].The ability to efficiently convert vibratory energy into electrical energy holds great promise for reducing dependence on external energy sources. Piezoelectric materials, acting as transducers that convert mechanical stimuli into electrical signals, have found widespread applications across various energy harvesting devices[2, 3], sensors[4] and actuators[5], spanning from macro to micro scales.

In contrast to piezoelectricity, which is confined to non-centrosymmetric materials and relies on strain, flexoelectricity stands out as an electromechanical phenomenon that couples electric fields with strain gradients and inversely induces mechanical strain by electric field gradients, demonstrating its prevalence across all dielectrics. Flexoelectricity was first predicted by Mashkevich and Tolpygo[6] in the 1950s and then observed experimentally by Scott[7]. Flexoelectricity can be considered as size-dependent electromechanical coupling due to the fact that its contribution becomes significant and even dominant at lower scales where the strain gradient effect becomes more profound as the material dimensions shrink to micro- and nano-levels. In its initial phases, flexoelectricity did not garner significant attention within the realm of hard materials, primarily owing to constraints in generating larger strain gradient. However, the domain of soft dielectric materials has revealed a broad spectrum of applications for flexoelectricity, such as biological membranes[8, 9, 10, 11], polymers[12, 13, 14] and liquid crystals[15, 16]. Reviews and discussions on flexoelectricity can be found e.g. in[17, 18, 19].

Macroscopic materials, typically stiff solids, face limitation in creating large strain gradients. Soft dielectrics have become a key focus of research due to their distinctive capability to undergo extensive deformations. This characteristic holds the potential for achieving more significant electric responses, attributed to the presence of larger strain gradients. The resulting mechanical deformations induced by applied electric fields create opportunities for applications such as flexible electronics, soft robotics, and sensing and actuation in various fields[20, 21, 22]. The design of innovative soft dielectric systems with enhanced performance involves the creation of specific architectures or microstructures, often requiring the application of numerical methods to address complex challenges across intricate geometries[23]. Clearly, the reduction of structural dimensions to the micro-and nanoscale facilitates nonlinearity, enabling the more accessible production of large strain gradients, thereby contributing to the increasing improvement of the flexoelectric effect.

The continuum theories of flexoelectricity in bulk solids have been explored[6, 15, 24, 25, 26], while a majority of these studies rely on the assumption of infinitesimal deformations, making them primarily applicable to modeling crystalline ceramics. The attempts to extend the theory to polymers or elastomers undergoing large deformations remains limited. In [10], Deng developed a nonlinear theoretical framework for flexoelectricity in soft materials. Liu[27] proposed an energy formulation for continuum electro-elasticity and magnetoelasticity. By applying the principle of minimum free energy, Euler-Lagrange equations were derived to encompass nonlinear dielectric effects with Maxwell contributions and flexoelectricity. Wang[28] developed a theoretical model incorporating both flexoelectricity and piezoelectricity for energy harvesting, accounting for geometric nonlinearity deformation and damping effects to more accurately predict the electromechanical behavior of energy harvesters. Some works have demonstrated that nonlinearity can significantly impact electromechanical coupling behavior of micro/nano structures[29, 30]. Additionally, exploring the nonlinear characteristics can be leveraged to enhance the performance of vibration energy harvesters[31, 32].

In numerical approaches, a challenge faced by the traditional finite element formulation when investigating the flexoelectric effect is the necessity for C^1 continuity to interpolate the strain gradient from the displacement variable. Several investigations have concentrated on addressing the fourth-order partial differential equations associated with flexoelectricity in solids. These efforts include analytical models applied to simplified geometries[25, 26, 33] and numerical techniques applied to more complex geometries [34, 35, 36, 37, 38, 39]. Recently, several studies have concentrated on tackling the complexities of flexoelectricity with large deformation. Yvonnet[23] proposed a numerical finite element framework aimed at modeling and solving the response of nonlinear soft dielectrics, considering the effects of Maxwell stress and flexoelectricity at finite strains, where the Argyris triangular elements were utilized to ensure C^1-continuity. Tran Quoc Thai[40] presented an isogeometric analysis for flexoelectricity in soft dielectric materials subjected to finite deformations, taking into account Maxwell stresses on the surface between two different media. After then, a staggered explicit-implicit isogeometric formulation based on large strain kinematics was proposed for soft dielectrics[41]. Codony[42] developed equilibrium equations describing the flexoelectric effect in soft dielectrics under large deformations based on isogeometric analysis. Deng[43] studied the impact of geometric nonlinearity on flexoelectricity in soft dielectrics under large deformation by using a mixed finite element formulation.

The intriguing challenges in the field of flexoelectricity revolve around the exploration of advanced materials featuring heightened flexoelectric properties and the creation of engineered structures that optimize electromechanical coupling through a synergistic utilization of both flexoelectric and piezoelectric effects. Various strategies have been suggested to enhance flexoelectric constants in solids, including the electrets[44] and architected materials[45, 46, 47, 48]. A more recent development involves the application of topology optimization (TO) as a promising method for enhancing apparent flexoelectricity and Electromechanical Coupling Factors in structures exhibiting both piezoelectric and flexoelectric characteristics. Topology optimization, boasting a lengthy and successful history in determining optimal material distribution to maximize specific properties[49], can be broadly categorized into two families: density-based methods and boundary-based methods. Density-based methods encompass the Solid Isotropic Material with Penalization (SIMP) method [49, 50, 51] and the Evolutionary Structural Optimization (ESO) method [52]. On the other hand, boundary-based methods include the Level Set Method (LSM)[53, 54], the phase field method [55] and Moving Morphable Components/Voids (MMC/V) method [56, 57]. More recently, there have been increasing attention on integrating machine learning/deep learning with topology optimization (see e.g.[58]). Among these mentioned methods, the SIMP method stands out for its simplicity of implementation and has been widely applied across numerous physical problems. TO has been applied to increase the apparent flexoelectric properties[59, 60], energy conversion in flexoelectric structures[61, 62, 63, 64, 65] and both[66]. Ortigosa[67] developed framework for the design of flexoelectric energy harvesters at finite strains using topology optimization. Zhuang[68] proposed a numerical framework for optimizing the energy converting factor for nonlinear geometric flexoelectric structures.

At the micro/nanoscale, the electromechanical coupling behaviors of nanostructures are notably influenced by both flexoelectricity and nonlinearity. Consequently, it becomes crucial to explore the structural configurations of soft dielectrics that fully leverage both flexoelectricity and nonlinearity to enhance the electromechanical coupling behaviors in micro/nano energy harvesters. In this paper, we propose a nonlinear topology optimization framework for the soft dielectrics at finite strain. A numerical framework for nonlinear dielectrics at finite strain is derived. The C^1-continuity is satisfied by Isogeometric analysis (IGA)[69, 70]. The procedure for consistent linearizations and IGA discretizations is presented. We put forward a novel and efficient strain density function (SDF) interpolation scheme, where the electromechanical and hyper-elastic energy terms are respectively interpolated based on SIMP model but the linear material density model is employed on dielectric one. As widely recognized, the essence of mechanical stiffness penalization is to ensure that the final topology converges to 1 or 0. However, the penalty for dielectric properties is not necessary. In our numerical analysis, we illustrate the good performance of the proposed SDF interpolation scheme in nonlinear electromechanical optimization scenarios. An energy remedy scheme[71] for void region is extended to optimization of soft dielectrics to avoid the distortion deformation in low-stiffness elements. The optimization solely based on the objective of the electromechanical coupling factor may lead to the formation of disconnected structures due to the neglect of mechanical stiffness considerations. To ensure the design of physically viable optimized structures, we incorporate a compliance constraint to regulate mechanical stiffness, thereby preventing the occurrence of disconnected domains. The influence of size effect on the optimization of flexoelectric soft materials is studied. In the numerical investigation, our proposed topology optimization framework for nonlinear flexoelectric soft materials fully leverages the interplay between size effect and larger deformation, resulting in a significant improvement in the electromechanical coupling factors within the optimized structures.

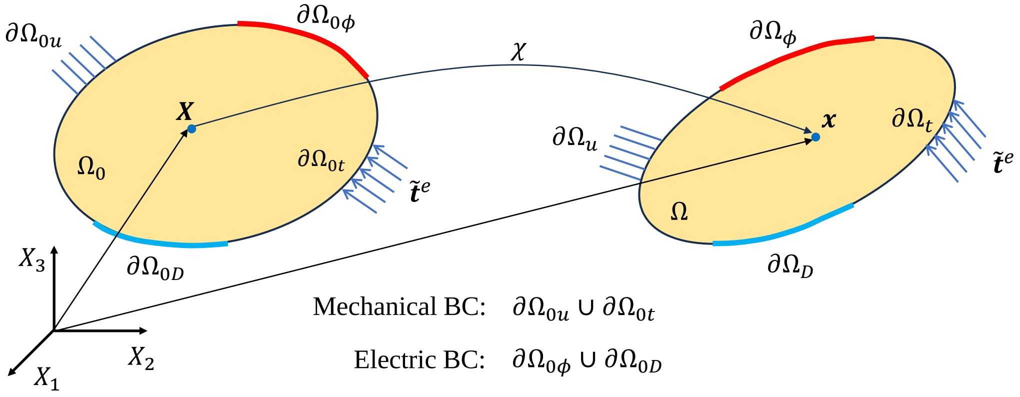

(a) (b)

Figure 1: A solid domain: (a) reference (undeformed) configuration; (b) current (deformed) configuration

2. Flexoelectricity for soft materials at finite strains

A solid domain $\Omega_0 \in \mathbb{R}^d$ is considered in the reference (undeformed) configuration, as schematically illustrated in Fig.1. The boundary $\partial\Omega_0$ of Ω_0 is composed of mechanical and electrostatic boundary. The mechanical boundary includes Dirichlet and Neumann portions, represented respectively by $\partial\Omega_{0u}$ and $\partial\Omega_{0t}$, where the displacement and traction are imposed such that $\partial\Omega_{0u} \cup \partial\Omega_{0t} = \partial\Omega_0$ and $\partial\Omega_{0u} \cap \partial\Omega_{0t} = \emptyset$. While the electrostatic one is composed of electric Dirichlet boundary $\partial\Omega_{0\phi}$ and Robin boundary $\partial\Omega_{0D}$, which are prescribed such that $\partial\Omega_{0\phi} \cup \partial\Omega_{0D} = \partial\Omega_0$ and $\partial\Omega_{0\phi} \cap \partial\Omega_{0D} = \emptyset$. The solid domain in current (deformed) configuration is denoted as Ω, and the counterparts of quantities are defined similarly by omitting the index 0. The deformation map $\chi : \Omega_0 \to \Omega$ maps every material point (or Lagrangian coordinate) $\boldsymbol{X} \in \Omega_0$ to the spatial point (or Eulerian coordinate) $\boldsymbol{x}$, i.e. $\boldsymbol{x} = \chi(\boldsymbol{X})$.

Here, the relevant quantities and notations are defined. The deformation gradient is defined as $\mathbf{F} = \nabla_X(\chi)$ and $\nabla_X(\cdot)$ denotes gradient with respect to reference configuration. $\mathbf{C} = \mathbf{F}^T\mathbf{F}$ is the right Cauchy-Green strain tensor. The Jacobian is defined as $J = \det(\mathbf{F})$. The divergence operator $Div = \nabla_X \cdot (\cdot)$ is related to reference configuration. The electric field, electric displacement, polarization and the first Piola-Kirchhoff stress in current configuration are denoted respectively as $\mathbf{E}$, $\mathbf{D}$, $\mathbf{P}$ and $\mathbf{\Sigma}$, while their counterparts in the reference configuration are expressed as $\tilde{\mathbf{E}}$, $\tilde{\mathbf{D}}$, $\tilde{\mathbf{P}}$ and $\tilde{\mathbf{\Sigma}}$, respectively. These quantities are related according to[27]:

$$\tilde{\mathbf{D}} = J\mathbf{F}^{-1}\mathbf{D}, \tilde{\mathbf{E}} = \mathbf{F}^T\mathbf{E}, \tag{1}$$

$$\tilde{\mathbf{\Sigma}} = J\mathbf{\Sigma}\mathbf{F}^{-T}, \tilde{\mathbf{P}} = J\mathbf{P} \tag{2}$$

and

$$\tilde{\mathbf{E}} = -\nabla_X \phi \tag{3}$$

$$\mathbf{F} = \mathbf{I} + \frac{\partial \mathbf{u}}{\partial \boldsymbol{X}} \tag{4}$$

with electric potential ϕ and unit matrix $\mathbf{I}$.

In this work, isotropic bulk flexoelectricity at finite strain is assumed, and surface effects are neglected. The total internal energy density of the system, encompassing contributions from elastic, flexoelectric, dielectric and linear gradient elastic portions, is provided as[23]:

$$\Psi = \Psi_{elast} + \Psi_{flexo} + \Psi_{diel} + \Psi_{elast}^{grad} \tag{5}$$

In this work, the Ψ_{elast} is considered as Mooney-Rivlin hyper-elastic model, and all the energy terms are given as

$$\Psi_{elast} = \frac{\mu}{2}(J^{-\frac{2}{3}}\Sigma_\alpha \lambda_\alpha^2 - 3) + \frac{\kappa}{2}(J-1)^2 \tag{6}$$

$$\Psi_{diel} = \frac{1}{2J}(\mathbf{R}^T \cdot \tilde{\mathbf{P}}) \cdot \mathbf{A} \cdot (\mathbf{R}^T \cdot \tilde{\mathbf{P}}) \tag{7}$$

$$\Psi_{flexo} = f_{ijkl}\tilde{P}_i G_{jkl} \tag{8}$$

$$\Psi_{elast}^{grad} = \frac{g_{ijklmn}}{2} G_{ijk} G_{lmn} \tag{9}$$

where μ and κ are the Lame's constants such that $\mu = \frac{E}{2(1+\nu)}$ and $\kappa = \frac{E}{3(1-2\nu)}$, with E being the Young's modulus and ν is Poisson's ratio. λ_α^2 $(\alpha = 1,2,3)$ is the eigenvalue of right Cauchy-Green tensor $\mathbf{C}$, $\mathbf{G}$ is second-order gradient of displacement, $\mathbf{G} = \nabla_X(\nabla_X(\mathbf{u}))$, $\mathbf{R}$ is the rotation tensor with the property $\mathbf{R}\cdot\mathbf{R}^T = \mathbf{I}$, f is a flexoelectric coefficient, g is a couple strain gradient constant and $\mathbf{A}$ is the second order dielectric tensor. For an isotropic dielectric medium, it is defined as

$$\mathbf{A} = \frac{1}{\varepsilon - \varepsilon_0}\mathbf{I} \tag{10}$$

where ε_0 is the vacuum electric permittivity.

By the principle of frame indifference, the energy functions Ψ_{flexo} and Ψ^{grad}_{elast} satisfy[27]:

$$\Psi_{flexo}(\mathbf{G},\tilde{\mathbf{P}}) = \Psi_{flexo}(\mathbf{RG},\mathbf{R}\tilde{\mathbf{P}}), \forall\mathbf{R} \in So(3) \tag{11}$$

$$\Psi^{grad}_{elast}(\mathbf{G},\mathbf{G}) = \Psi^{grad}_{elast}(\mathbf{RG},\mathbf{RG}), \forall\mathbf{R} \in So(3) \tag{12}$$

where $So(3) \subset \mathbb{R}^{3\times 3}$ is the group consisting of all rigid rotations. Then using the property of the material symmetry, we have

$$\Psi_{flexo}(\mathbf{G},\tilde{\mathbf{P}}) = \Psi_{flexo}(\mathbf{RG}',\mathbf{R}\tilde{\mathbf{P}}'), \forall\mathbf{Q} \in \mathcal{G} \tag{13}$$

$$\Psi^{grad}_{elast}(\mathbf{G},\mathbf{G}) = \Psi^{grad}_{elast}(\mathbf{RG}',\mathbf{RG}'), \forall\mathbf{Q} \in \mathcal{G} \tag{14}$$

where $\mathbf{G}'_{ijk} = \mathbf{G}_{imn}Q_{mj}Q_{nk}$ and $\tilde{\mathbf{P}}'_i = \tilde{\mathbf{P}}_jQ_{ji}$. Let $\mathcal{G} \subset \mathbb{R}^{3\times 3}$ be the material symmetry group. For isotropic medium, i.e. $\mathcal{G} = So(3)$, any isotropic tensor, as well as higher-order tensors such as f_{ijkl} and g_{ijklmn}, can be represented as linear combinations of some isomers[72]. The general bilinear forms that fulfill the above identity (11)-(14) have been systematically derived in [72]. For simplicity, special forms for Ψ_{flexo} and Ψ^{grad}_{elast} with a single parameter, employed in [27] are used here:

$$\Psi_{flexo} = f\tilde{P}_iG_{ikk} \tag{15}$$

$$\Psi^{grad}_{elast} = \frac{g}{2}G_{ikk}G_{ill} \tag{16}$$

The first Piola-Kirchhoff stress $\tilde{\mathbf{\Sigma}}$ is expressed by:

$$\tilde{\mathbf{\Sigma}} = \frac{\partial\Psi_{elast}}{\partial\mathbf{F}} = -\frac{\mu}{3}J^{-\frac{2}{3}}\mathbf{F}^{-T}\Sigma_\alpha\lambda_\alpha^2 + \mu J^{-\frac{2}{3}}\mathbf{F} + \kappa(J-1)J\mathbf{F}^{-T} \tag{17}$$

The third-order hyperstress $\mathcal{S}$ is defined as

$$\begin{aligned}\mathcal{S}_{ijk} = \frac{\partial\Psi}{\partial G_{ijk}} &= \frac{g}{2}\delta_{mi}\delta_{kj}G_{mll} + \frac{g}{2}G_{mnn}\delta_{mi}\delta_{kj} + f\tilde{P}_m\delta_{mi}\delta_{jk} \\ &= gG_{ill}\delta_{jk} + f\tilde{P}_i\delta_{jk}\end{aligned} \tag{18}$$

where δ_{ij} is Kronecker delta.

The mechanical and electric equilibrium equations for flexoelectricity with boundary conditions are defined as[27]

$$\begin{cases} \mathbf{F}^{-T}\nabla_X\phi + \frac{\partial\Psi}{\partial\tilde{\mathbf{P}}} = 0 \ in \ \Omega_0 \\ Div\ \tilde{\mathbf{D}} = \tilde{\rho}^e \ in \ \Omega_0, \ \tilde{\mathbf{D}} = -\varepsilon_0 J\mathbf{C}^{-1}\nabla_X\phi + \mathbf{F}^{-1}\tilde{\mathbf{P}} \\ Div(Div\frac{\partial\Psi}{\partial\mathbf{G}}) - Div\frac{\partial\Psi}{\partial\mathbf{F}} - \tilde{\mathbf{f}}^e = 0 \ in \ \Omega_0 \end{cases} \tag{19}$$

with

$$\begin{cases} (\frac{\partial\Psi}{\partial\mathbf{F}})\mathbf{N} - (Div\ \frac{\partial\Psi}{\partial\mathbf{G}})\mathbf{N} - \tau - \tilde{\mathbf{t}}^e = 0 \ on \ \partial\Omega_0 \\ (\frac{\partial\Psi}{\partial\mathbf{G}})\mathbf{N}\otimes\mathbf{N} = 0 \ on \ \partial\Omega_0 \end{cases} \tag{20}$$

where $\mathbf{N}$ is the unitary normal vector to the boundary $\partial\Omega_0$. $\tilde{\mathbf{f}}^e$ and $\tilde{\mathbf{t}}^e$ denote body force and traction, respectively. The components of the vector field τ are given by [27]:

$$\tau_k = [\mathcal{S}_{kij}N_j(\delta_{im} - N_iN_m)]_{,m} - [\mathcal{S}_{kij}N_j - N_iN_m]_{,n}N_nN_m \tag{21}$$

Here, $\boldsymbol{\tau} = \mathbf{0}$. According to (7), we can obtain

$$\frac{\partial\Psi}{\partial\tilde{\mathbf{P}}} = \frac{1}{J}\mathbf{R}\mathbf{A}\mathbf{R}^T\tilde{\mathbf{P}} \tag{22}$$

Substituting (10) and (22) into the first formula of (19), we have

$$\tilde{\mathbf{P}} = -J(\mathbf{R}\mathbf{A}\mathbf{R}^T)^{-1}[fG_{ikk} + \mathbf{F}^{-T}\nabla_X\phi] = -J(\varepsilon - \varepsilon_0)(fG_{ikk} + \mathbf{F}^{-T}\nabla_X\phi) \tag{23}$$

From the second row of (19) and (23), then omitting the term $\tilde{\mathbf{P}}^e$, we arrive at

$$\tilde{\mathbf{D}} = -J\varepsilon\mathbf{C}^{-1}\nabla_X\phi - Jf(\varepsilon - \varepsilon_0)\mathbf{F}^{-1}G_{ikk} \tag{24}$$

The strong forms of the boundary values problems are provided as follows. The dielectric problem with Dirichlet and/or Robin boundary conditions is defined as:

$$\begin{cases} \nabla_X \cdot \tilde{\mathbf{D}} = \tilde{\rho}^e \ in \ \Omega_0 \\ \phi = \phi^e \ on \ \partial\Omega_{0\phi} \\ \tilde{N} \cdot \tilde{\mathbf{D}} = D^b \ on \ \partial\Omega_{0D} \end{cases} \tag{25}$$

The mechanical problem with Dirichlet and Neumann boundary conditions is expressed as:

$$\begin{cases} \nabla_X \cdot \tilde{\boldsymbol{\Sigma}} - \nabla_X \cdot (\nabla_X \cdot \mathcal{S}) + \tilde{\mathbf{f}}^e = 0, \ in \ \Omega_0 \\ \boldsymbol{\Sigma} \cdot \tilde{\mathbf{N}} - (\nabla_X \cdot \mathcal{S}) \cdot \tilde{\mathbf{N}} - \tilde{\mathbf{t}} = 0 \ on \ \partial\Omega_{0t} \\ \mathcal{S}\tilde{\mathbf{N}} \otimes \tilde{\mathbf{N}} = 0 \ on \ \partial\Omega_0 \\ u = u^b \ on \ \partial\Omega_{0u} \end{cases} \tag{26}$$

3. Weak forms of flexoelectric equilibrium equations

To be handled by discrete numerical methods, such as IGA method employed here, the above boundary values problem defined in (25)-(26) must be recast into weak forms. The weak formulations for electric and mechanical equilibrium are derived by employing the principle of virtual work. The electric potential is defined as $\phi \in \{\phi = \bar{\phi}^* \text{ on } \partial\Omega_{0\phi}, \phi \in H^1(\Omega_0)\}$ and its corresponding test function as $\delta\phi \in \{\phi = 0 \text{ on } \partial\Omega_{0\phi}, \phi \in H^1(\Omega_0)\}$. Multiplying the first row of (25) by the test function $\delta\phi$ and integrating over Ω_0, we obtain the dielectric problem as

$$\int_{\Omega_0} \nabla_X \cdot \tilde{\mathbf{D}} \cdot \delta\phi d\Omega_0 = \int_{V_0} \tilde{\rho}^e \cdot \delta\phi d\Omega_0 \tag{27}$$

By using the divergence theorem, we have

$$\int_{\Omega_0} -\tilde{\mathbf{D}} \cdot \nabla_X(\delta\phi) d\Omega_0 = \int_{\Omega_0} \tilde{\rho}^e \delta\phi d\Omega_0 - \int_{\partial\Omega_0} \tilde{\mathbf{D}} \cdot \mathbf{N} \delta\phi d\Omega_0 \tag{28}$$

As $\phi = 0$ on $\partial\Omega_{0\phi}$, introducing the last two rows of (25), we obtain

$$\int_{\Omega_0} -\tilde{\mathbf{D}} \cdot \nabla_X(\delta\phi) d\Omega_0 = \int_{\Omega_0} \tilde{\rho}^e \delta\phi d\Omega_0 - \int_{\partial\Omega_{0D}} D^b \delta\phi d\Omega_0 \tag{29}$$

Substituting (24) into (29), we arrive at

$$\int_{\Omega_0} J\varepsilon \mathbf{C}^{-1} \nabla_X \phi \cdot \nabla_X(\delta\phi) d\Omega_0 + \int_{V_0} Jf(\varepsilon - \varepsilon_0) \mathbf{F}^{-1} G_{ikk} \cdot \nabla_X(\delta\phi) d\Omega_0$$

$$= \int_{\Omega_0} \tilde{\rho}^e \delta\phi - \int_{\partial\Omega_{0D}} D^b \delta\phi d\Omega_0 \tag{30}$$

In the mechanical problem, we assume the displacement $\mathbf{u} \in \{\mathbf{u} = \bar{\mathbf{u}}^* \text{ on } \partial\Omega_{0u}, \mathbf{u} \in H^2(\Omega_0)\}$. Multiplying the first equation in (26) by the test function $\delta\mathbf{u} \in \{\mathbf{u} = 0 \text{ on } \partial\Omega_{0u}, \mathbf{u} \in H^2(\Omega_0)\}$, integrating over Ω_0, we have

$$\int_{\Omega_0} \nabla_X \cdot \tilde{\boldsymbol{\Sigma}} \cdot \delta\mathbf{u} d\Omega_0 - \int_{\Omega_0} \nabla_X \cdot (\nabla_X \cdot \mathcal{S}) \cdot \delta\mathbf{u} d\Omega_0 + \int_{\Omega_0} \tilde{\mathbf{f}} \delta\mathbf{u} d\Omega_0 = 0 \tag{31}$$

Using integral by part, we obtain

$$\int_{\Omega_0} \nabla_X \cdot (\tilde{\boldsymbol{\Sigma}} \delta \mathbf{u}) d\Omega_0 - \int_{\Omega_0} \tilde{\boldsymbol{\Sigma}} : \nabla_X \delta \mathbf{u} d\Omega_0 - \int_{\Omega_0} \nabla_X \cdot ((\nabla_X \cdot \mathcal{S}) \delta \mathbf{u}) d\Omega_0 \\ + \int_{\Omega_0} (\nabla_X \cdot \mathcal{S}) : \nabla_X \delta \mathbf{u} d\Omega_0 + \int_{\Omega_0} \tilde{\mathbf{f}} \cdot \delta \mathbf{u} d\Omega_0 = 0 \tag{32}$$

By Gauss's theorem and $\nabla_X \delta \mathbf{u} = \delta \mathbf{F}$, we have

$$\int_{\Omega_0} \tilde{\boldsymbol{\Sigma}} : \delta \mathbf{F} d\Omega_0 - \int_{\Omega_0} (\nabla_X \cdot \mathcal{S}) : \delta \mathbf{F} d\Omega_0 = \int_{\Omega_0} \tilde{\mathbf{f}} \cdot \delta \mathbf{u} d\Omega_0 + \int_{\partial\Omega_0} (\tilde{\boldsymbol{\Sigma}} \mathbf{N} - \nabla_X \cdot \mathcal{S} \mathbf{N}) \cdot \delta \mathbf{u} d\Omega_0 \tag{33}$$

Considering the boundary condition defined in the second row of (26), it yields:

$$\int_{\Omega_0} \tilde{\boldsymbol{\Sigma}} : \delta \mathbf{F} d\Omega_0 - \int_{\Omega_0} (\nabla_X \cdot \mathcal{S}) : \delta \mathbf{F} d\Omega_0 = \int_{\Omega_0} \tilde{\mathbf{f}} \cdot \delta \mathbf{u} d\Omega_0 + \int_{\partial\Omega_{0t}} \tilde{\mathbf{t}} \cdot \delta \mathbf{u} d\Omega_0 \tag{34}$$

The third-order tensor $\mathcal{U}$ and second-order tensor $\mathbf{V}$ have the property $\nabla \cdot (\mathcal{U} : \mathbf{V}) = (\nabla \cdot \mathcal{U}) : \mathbf{V} + \mathcal{U} \vdots \nabla \mathbf{V}$. By introducing this property into the second term of (34), we obtain

$$\int_{\Omega_0} \tilde{\boldsymbol{\Sigma}} : \delta \mathbf{F} d\Omega_0 + \int_{\Omega_0} \mathcal{S} \vdots \delta \mathbf{G} d\Omega_0 - \int_{\partial\Omega_0} \mathcal{S} \mathbf{N} : \delta \mathbf{F} d\Omega_0 = \int_{\Omega_0} \tilde{\mathbf{f}} \cdot \delta \mathbf{u} d\Omega_0 + \int_{\partial\Omega_{0t}} \tilde{\mathbf{t}} \cdot \delta \mathbf{u} d\Omega_0 \tag{35}$$

Assuming the boundary condition $\mathcal{S}\mathbf{N} = 0$ on $\partial\Omega_0$, we finally obtain the weak form of the mechanical equilibrium equation as:

$$\int_{\Omega_0} \tilde{\boldsymbol{\Sigma}} : \delta \mathbf{F} d\Omega_0 + \int_{\Omega_0} \mathcal{S} \vdots \delta \mathbf{G} d\Omega_0 = \int_{\Omega_0} \tilde{\mathbf{f}} \cdot \delta \mathbf{u} d\Omega_0 + \int_{\partial\Omega_{0t}} \tilde{\mathbf{t}} \cdot \delta \mathbf{u} dS \tag{36}$$

4. Consistent linearization of flexoelectric weak-form equations

The linearization is as follow. The residuals are calculated by,

$$\begin{cases} \mathbf{R}_\phi(\mathbf{u}, \phi) = \mathbf{q}(\mathbf{u}, \phi) - \mathbf{q}^{ext} = 0 \\ \mathbf{R}_u(\mathbf{u}, \phi) = \mathbf{f}(\mathbf{u}, \phi) - \mathbf{f}^{ext} = 0 \end{cases} \tag{37}$$

where

$$
\begin{aligned}
\mathbf{q}(\mathbf{u},\phi) &= \int_{\Omega_0} -\tilde{\mathbf{D}}\cdot\nabla_X(\delta\phi)d\Omega_0 \\
&= \int_{V_0} J\varepsilon\mathbf{C}^{-1}\nabla_X(\delta\phi)\cdot\nabla_X\phi dV_0 + \int_{V_0} Jf(\varepsilon-\varepsilon_0)\mathbf{F}^{-1}G_{ikk}\cdot\nabla_X(\delta\phi)d\Omega_0
\end{aligned}
\tag{38}
$$

$$
\mathbf{f}(\mathbf{u},\phi) = \int_{\Omega_0}\tilde{\mathbf{\Sigma}} : \delta\mathbf{F}d\Omega_0 + \int_{\Omega_0}\mathcal{S}\vdots\delta\mathbf{G}d\Omega_0 \tag{39}
$$

$$
\mathbf{q}^{ext} = \int_{\Omega_0}\tilde{\rho}^e\delta\phi d\Omega_0 - \int_{\partial\Omega_{0D}} D^b\delta\phi d\Omega_0 \tag{40}
$$

$$
\mathbf{f}^{ext} = \int_{\Omega_0}\tilde{\mathbf{f}}\cdot\delta\mathbf{u}d\Omega_0 + \int_{\partial\Omega_0}\tilde{\mathbf{t}}\cdot\delta\mathbf{u}d\Omega_0 \tag{41}
$$

Their Taylor expansions are respectively given as

$$
\begin{cases}
\mathbf{R}_\phi(\mathbf{u}+\Delta\mathbf{u},\phi+\Delta\phi) = \mathbf{R}_\phi(\mathbf{u},\phi) + D_{\Delta\mathbf{u}}\mathbf{R}_\phi(\mathbf{u},\phi) + D_{\Delta\phi}\mathbf{R}_\phi(\mathbf{u},\phi) = 0 \\
\mathbf{R}_u(\mathbf{u}+\Delta\mathbf{u},\phi+\Delta\phi) = \mathbf{R}_u(\mathbf{u},\phi) + D_{\Delta\mathbf{u}}\mathbf{R}_u(\mathbf{u},\phi) + D_{\Delta\phi}\mathbf{R}_u(\mathbf{u},\phi) = 0
\end{cases}
\tag{42}
$$

The solution for the next increment in an iterative Newton-like procedure consists in solving the linearized problems for $\Delta\mathbf{u}$ and $\Delta\phi$ and to update the field variables for the next iteration through $\mathbf{u}^{k+1} = \mathbf{u}^k + \Delta\mathbf{u}$ and $\phi^{k+1} = \phi^k + \Delta\phi$. For the sake of clarity, the superscript k is omitted. Let us group all unknown quantities, respectively the displacement vector $\mathbf{u}$ and the potential ϕ in a vector $\mathbf{v}$. The directional derivatives of $f(\mathbf{v})$ in the direction of $\Delta\mathbf{v}$ is defined as:

$$
D_{\Delta\mathbf{v}}f(\mathbf{v}) = \left[\frac{d}{d\alpha}\{f(\mathbf{v}+\alpha\Delta\mathbf{v})\}\right]_{\alpha=0} \tag{43}
$$

We obtain $\Delta\mathbf{F} = \nabla_X(\Delta\mathbf{u})$ and $\Delta\mathbf{G} = \nabla_X(\nabla_X(\Delta\mathbf{u}))$. Thus, the directional derivatives of the residuals $\mathbf{R}(\mathbf{u},\phi) = [\mathbf{R}_\phi(\mathbf{u},\phi);\mathbf{R}_u(\mathbf{u},\phi)]$ with respect to $\Delta\phi$ and $\Delta\mathbf{u}$ are provided, respectively, as

$$
\begin{cases}
D_{\Delta\phi}\mathbf{R}(\mathbf{u},\phi) = \frac{\partial\mathbf{R}}{\partial\phi}\Delta\phi = \frac{\partial\mathbf{R}}{\partial\nabla_X\phi}\frac{\partial\nabla_X\phi}{\partial\phi}\Delta\phi = \frac{\partial\mathbf{R}_\phi}{\partial\nabla_X\phi}\nabla_X(\Delta\phi) \\
D_{\Delta\mathbf{u}}\mathbf{R}(\mathbf{u},\phi) = \frac{\partial\mathbf{R}}{\partial\mathbf{u}}\Delta\mathbf{u} = \frac{\partial\mathbf{R}}{\partial\mathbf{F}}\frac{\partial\mathbf{F}}{\partial\mathbf{u}}\Delta\mathbf{u} + \frac{\partial\mathbf{R}}{\partial\mathbf{G}}\frac{\partial\mathbf{G}}{\partial\mathbf{u}}\Delta\mathbf{u} = \frac{\partial\mathbf{R}}{\partial\mathbf{F}}\Delta\mathbf{F} + \frac{\partial\mathbf{R}}{\partial\mathbf{G}}\Delta\mathbf{G}
\end{cases}
\tag{44}
$$

Substituting (37)-(42) into (44) and assuming constant external forces (dead loads), we obtain

$$\begin{cases} D_{\Delta\phi}\mathbf{R}_{\phi}(\mathbf{u},\phi) = \int_{\Omega_0} \nabla_X(\delta\phi)\cdot\frac{\partial(-\tilde{\mathbf{D}})}{\partial\nabla_X\phi}\cdot\nabla_X(\Delta\phi)d\Omega_0 \\ D_{\Delta\mathbf{u}}\mathbf{R}_{\phi}(\mathbf{u},\phi) = \int_{\Omega_0}\{\nabla_X(\delta\phi)\cdot\frac{\partial(-\tilde{\mathbf{D}})}{\partial\mathbf{F}} : \Delta\mathbf{F} + \nabla_X(\delta\phi)\cdot\frac{\partial(-\tilde{\mathbf{D}})}{\partial\mathbf{G}}\vdots\Delta\mathbf{G}\}d\Omega_0 \end{cases} \tag{45}$$

and

$$\begin{cases} D_{\Delta\phi}\mathbf{R}_{u}(\mathbf{u},\phi) = \int_{\Omega_0} \delta\mathbf{G}\vdots\frac{\partial\mathcal{S}}{\partial\nabla_X\phi}\cdot\nabla_X(\Delta\phi)d\Omega_0 \\ D_{\Delta\mathbf{u}}\mathbf{R}_{u}(\mathbf{u},\phi) = \int_{\Omega_0}\delta\mathbf{F} : \frac{\partial\tilde{\mathbf{\Sigma}}}{\partial\mathbf{F}} : \Delta\mathbf{F}d\Omega_0 + \int_{\Omega_0}\delta\mathbf{G}\vdots\frac{\partial\mathcal{S}}{\partial\mathbf{F}} : \Delta\mathbf{F}d\Omega_0 + \int_{\Omega_0}\delta\mathbf{G}\vdots\frac{\partial\mathcal{S}}{\partial\mathbf{G}}\vdots\Delta\mathbf{G}d\Omega_0 \end{cases} \tag{46}$$

Here, we recall the derivatives of deformation gradient $\mathbf{F}$, inverse deformation gradient $\mathbf{F}^{-1}$ and the right Cauchy-Green strain with respect to the deformation gradient that will be used in the following formulas:

$$\mathbb{F}_{ijkl} = \frac{\partial F^{-1}_{ij}}{\partial F_{kl}} = -F^{-1}_{ik}F^{-1}_{lj} \tag{47}$$

$$\tilde{\mathbb{F}}_{ijkl} = \frac{\partial F^{-T}_{ij}}{\partial F_{kl}} = -F^{-1}_{li}F^{-1}_{jk} \tag{48}$$

$$\tilde{\mathbb{A}}_{ijkl} = \frac{\partial C^{-1}_{ij}}{\partial F_{kl}} = -F^{-1}_{ik}C^{-1}_{jl} - C^{-1}_{il}F^{-1}_{jk} \tag{49}$$

For the polarization defined in (23), its derivatives with respect to the deformation gradient $\mathbf{F}$, electric potential gradient $\nabla_X\phi$ and the second-order gradient of displacement $\mathbf{G}$ can be obtained as:

$$\begin{cases} \frac{\partial\tilde{P}_i}{\nabla_m\phi} = -J(\varepsilon-\varepsilon_0)F^{-1}_{mi} \\ \frac{\partial\tilde{P}_i}{\partial F_{kl}} = -J(\varepsilon-\varepsilon_0)(fF^{-1}_{lk}G_{ipp} + F^{-1}_{lk}F^{-1}_{mi}\nabla_m\phi + \tilde{\mathbb{F}}_{imkl}\nabla_m\phi) \\ \frac{\partial\tilde{P}_i}{\partial G_{jkl}} = -J(\varepsilon-\varepsilon_0)f\delta_{ij}\delta_{kl} \end{cases} \tag{50}$$

The electric displacement in (24) with respect to the three fields $\mathbf{F}$, $\nabla_X\phi$ and $\mathbf{G}$, is derived according to:

$$\begin{cases} \frac{\partial\tilde{D}_i}{\partial\nabla_m\phi} = -J\varepsilon C^{-1}_{im} \\ \frac{\partial\tilde{D}_i}{\partial F_{kl}} = -J\varepsilon(F^{-1}_{lk}C^{-1}_{im} - F^{-1}_{ik}C^{-1}_{ml} - C^{-1}_{il}F^{-1}_{mk})\nabla_m\phi - Jf(\varepsilon-\varepsilon_0)(F^{-1}_{im}F^{-1}_{lk} + \mathbb{F}_{imkl})G_{mpp} \\ \frac{\partial\tilde{D}_i}{\partial G_{jkl}} = -Jf(\varepsilon-\varepsilon_0)F^{-1}_{ij}\delta_{kl} \end{cases} \tag{51}$$

We obtain the derivatives of hyperstress given in (18) as:

$$\begin{cases} \frac{\partial \mathcal{S}_{ijk}}{\partial \nabla_l \phi} = -Jf(\varepsilon-\varepsilon_0)F^{-1}_{li}\delta_{jk} \\ \frac{\partial \mathcal{S}_{ijk}}{\partial F_{lm}} = -f\delta_{jk}J(\varepsilon-\varepsilon_0)(fF^{-1}_{ml}G_{ipp}+F^{-1}_{ml}F^{-1}_{ni}\nabla_n\phi-F^{-1}_{mi}F^{-1}_{nl}\nabla_n\phi) \\ \frac{\partial \mathcal{S}_{ijk}}{\partial G_{lmn}} = g\delta_{il}\delta_{jk}\delta_{mn}-Jf^2(\varepsilon-\varepsilon_0)\delta_{il}\delta_{jk}\delta_{mn} \end{cases} \tag{52}$$

As the first Piola-Kirchhoff stress defined in (17) is only related to the deformation gradient $\mathbf{F}$, then we have

$$\begin{aligned} \frac{\partial \tilde{\Sigma}_{ij}}{\partial F_{kl}} = & \frac{2\mu}{9}J^{-\frac{2}{3}}F^{-1}_{ji}F^{-1}_{lk}\Sigma_\alpha\lambda_\alpha^2+\frac{\mu}{3}J^{-\frac{2}{3}}F^{-1}_{li}F^{-1}_{jk}\Sigma_\alpha\lambda_\alpha^2 \\ & -\frac{2\mu}{3}J^{-\frac{2}{3}}F^{-1}_{ji}F_{kl}-\frac{2\mu}{3}J^{-\frac{2}{3}}F^{-1}_{lk}F_{ij}+\mu J^{-\frac{2}{3}}\delta_{ik}\delta_{jl} \\ & +\kappa(2J-1)JF^{-1}_{ji}F^{-1}_{lk}-\kappa(J-1)JF^{-1}_{li}F^{-1}_{jk} \end{aligned} \tag{53}$$

5. IGA Discretization

The fundamental concept of isogeometric analysis is the use of NURBS not only as a means of discretizing geometry, but also as a tool for discretizing partial differential equations[69, 70]. The NURBS basis functions with higher continuity are employed here to solve the fourth-order flexoelectric PDEs. For the sake of simplicity, we restrict the developments to 2D, even though extension to 3D is straightforward. The basis function for NURBS surfaces is defined as:

$$R^{p,q}_{i,j}(\xi,\eta)=\frac{N_{i,p}(\xi)M_{j,q}(\eta)w_{i,j}}{\sum_{\hat{i}=1}^{n}\sum_{\hat{j}=1}^{m}N_{\hat{i},p}(\xi)M_{\hat{j},q}(\eta)w_{\hat{i},\hat{j}}} \tag{54}$$

where the knots $\boldsymbol{\xi}=\{\xi_1,\xi_2,...,\xi_{n+p+1}\}$, $\boldsymbol{\eta}=\{\eta_1,\eta_2,...,\eta_{m+q+1}\}$, p and q are the polynomial orders, n and m are the number of basis function, $w_{i,j}$ are positive weights, $N_{i,p}(\xi)$ and $M_{i,q}(\eta)$ are univariate B-Spline basis of order p and q corresponding to knot vectors $\boldsymbol{\xi}$ and $\boldsymbol{\eta}$, respectively, and are recursively defined as[73]

$$N_{i,0}=\begin{cases} 0, & if\ \xi_i \le \xi \le \xi_{i+1} \\ 1, & \text{otherwise.} \end{cases} \tag{55}$$

and for $p = 1, 2, ...$, we have

$$N_{i,p}(\xi) = \frac{\xi - \xi_i}{\xi_{i+p} - \xi_i} N_{i,p-1}(\xi) + \frac{\xi_{i+p+1} - \xi}{\xi_{i+p+1} - \xi_{i+1}} N_{i+1,p-1}(\xi) \tag{56}$$

The polynomial orders of NURBS mesh are chosen as $p = q = 3$ for all numerical cases. The discretization of the electric potential ϕ and displacement $\mathbf{u}$ can be defined as

$$\phi(\mathbf{x}) = \sum_{i=1}^{n} \sum_{j=1}^{m} R_{i,j}^{p,q}(\xi, \eta) \phi^e = \mathbf{N}_\phi \phi^e \tag{57}$$

$$\mathbf{u}(\mathbf{x}) = \sum_{i=1}^{n} \sum_{j=1}^{m} R_{i,j}^{p,q}(\xi, \eta) u_{ij}^e = \mathbf{N}_u \mathbf{u}^e \tag{58}$$

The test function, potential increment and their corresponding gradient are approximated by

$$\begin{aligned} &\delta\phi = \mathbf{N}_\phi \delta\phi^e,\ \Delta\phi = \mathbf{N}_\phi \Delta\phi^e \\ &\nabla_X(\delta\phi) = \mathbf{B}_\phi \delta\phi^e,\ \nabla_X(\Delta\phi) = \mathbf{B}_\phi \Delta\phi^e \end{aligned} \tag{59}$$

Similarly, the test function, displacement increment and their corresponding gradient are obtained as:

$$\begin{aligned} &\delta\mathbf{u} = \mathbf{N}_u \delta\mathbf{u}^e,\ \Delta\mathbf{u} = \mathbf{N}_u \Delta\mathbf{u}^e \\ &\delta\mathbf{F} = \mathbf{B}_u \delta\mathbf{u}^e,\ \Delta\mathbf{F} = \mathbf{B}_u \Delta\mathbf{u}^e \end{aligned} \tag{60}$$

The vector forms of deformation gradient tensor and strain gradient are given, respectively, by

$$[\Delta\mathbf{F}] = \begin{bmatrix} \Delta F_{11} \\ \Delta F_{21} \\ \Delta F_{12} \\ \Delta F_{22} \end{bmatrix} = \begin{bmatrix} \frac{\partial \Delta u_1}{\partial X_1} \\ \frac{\partial \Delta u_2}{\partial X_1} \\ \frac{\partial \Delta u_1}{\partial X_2} \\ \frac{\partial \Delta u_2}{\partial X_2} \end{bmatrix} \tag{61}$$

and

$$[\mathbf{G}(\Delta\mathbf{u})] = \begin{bmatrix} G_{111}(\Delta\mathbf{u}) \\ G_{112}(\Delta\mathbf{u}) \\ G_{211}(\Delta\mathbf{u}) \\ G_{122}(\Delta\mathbf{u}) \\ G_{212}(\Delta\mathbf{u}) \\ G_{222}(\Delta\mathbf{u}) \end{bmatrix} = \begin{bmatrix} \frac{\partial^2 \Delta u_1}{\partial X_1^2} \\ \frac{\partial^2 \Delta u_1}{\partial X_1 \partial X_2} \\ \frac{\partial^2 \Delta u_2}{\partial X_1^2} \\ \frac{\partial^2 \Delta u_1}{\partial X_2^2} \\ \frac{\partial^2 \Delta u_2}{\partial X_1 \partial X_2} \\ \frac{\partial^2 \Delta u_2}{\partial X_2^2} \end{bmatrix} \tag{62}$$

Then the discrete form of the strain gradient is obtained as:

$$[\mathbf{G}(\Delta\mathbf{u})] = \mathbf{H}_u \Delta\mathbf{u}^e, \ [\delta\mathbf{G}] = \mathbf{H}_u \delta\mathbf{u}^e \tag{63}$$

Above, $\mathbf{N}_\phi = \mathbf{N}_u$ are the discrete interpolation shape functions, their gradients $\mathbf{B}_\phi$ and $\mathbf{B}_u$, and second gradient $\mathbf{H}_u$. These matrices are defined as (n is the number of control points for every element):

$$\mathbf{B}_\phi = \begin{bmatrix} \frac{\partial N_\phi^1}{\partial X_1} & \cdots & \frac{\partial N_\phi^n}{\partial X_1} \\ \frac{\partial N_\phi^1}{\partial X_2} & \cdots & \frac{\partial N_\phi^n}{\partial X_2} \end{bmatrix}, \ \mathbf{B}_u = \begin{bmatrix} \frac{\partial N_u^1}{\partial X_1} & \cdots & \frac{\partial N_u^n}{\partial X_1} & 0 & \cdots, & 0 \\ 0 & \cdots & 0 & \frac{\partial N_u^1}{\partial X_1} & \cdots & \frac{\partial N_u^n}{\partial X_1} \\ \frac{\partial N_u^1}{\partial X_2} & \cdots & \frac{\partial N_u^n}{\partial X_2} & 0 & \cdots, & 0 \\ 0 & \cdots & 0 & \frac{\partial N_u^1}{\partial X_2} & \cdots & \frac{\partial N_u^n}{\partial X_2} \end{bmatrix} \tag{64}$$

$$\mathbf{H}_u = \begin{bmatrix} \frac{\partial^2 N_u^1}{\partial X_1^2} & \cdots & \frac{\partial^2 N_u^n}{\partial X_1^2} & 0 & \cdots & 0 \\ \frac{\partial^2 N_u^1}{\partial X_1 \partial X_2} & \cdots & \frac{\partial^2 N_u^n}{\partial X_1 \partial X_2} & 0 & \cdots & 0 \\ 0 & \cdots & 0 & \frac{\partial^2 N_u^1}{\partial X_1^2} & \cdots & \frac{\partial^2 N_u^n}{\partial X_1^2} \\ \frac{\partial^2 N_u^1}{\partial X_1^2} & \cdots & \frac{\partial^2 N_u^n}{\partial X_1^2} & 0 & \cdots & 0 \\ 0 & \cdots & 0 & \frac{\partial^2 N_u^1}{\partial X_1 \partial X_2} & \cdots & \frac{\partial^2 N_u^n}{\partial X_1 \partial X_2} \\ 0 & \cdots & 0 & \frac{\partial^2 N_u^1}{\partial X_2^2} & \cdots & \frac{\partial^2 N_u^n}{\partial X_2^2} \end{bmatrix} \tag{65}$$

Introducing the approximation (57)-(60) and (63) into (45)-(46), then substituting into (42), we finally obtain the discrete form of the linearized equations:

$$\begin{bmatrix} \mathbf{K}_{\phi\phi}(\phi,\mathbf{u}) & \mathbf{K}_{\phi u}(\phi,\mathbf{u}) \\ \mathbf{K}_{u\phi}(\phi,\mathbf{u}) & \mathbf{K}_{uu}(\phi,\mathbf{u}) \end{bmatrix} \begin{bmatrix} \Delta\phi \\ \Delta\mathbf{u} \end{bmatrix} = - \begin{bmatrix} \mathbf{R}_\phi(\phi,\mathbf{u}) \\ \mathbf{R}_u(\phi,\mathbf{u}) \end{bmatrix} \tag{66}$$

where

$$\mathbf{K}_{\phi\phi}(\phi,\mathbf{u}) = \int_{\Omega_0} \mathbf{B}_{\phi}^{T} \frac{\partial(-\tilde{\mathbf{D}})}{\partial \nabla \phi} \mathbf{B}_{\phi} d\Omega_0 \tag{67}$$

$$\mathbf{K}_{\phi u}(\phi,\mathbf{u}) = \int_{\Omega_0} \left\{ \mathbf{B}_{\phi}^{T} \frac{\partial(-\tilde{\mathbf{D}})}{\partial \mathbf{F}} \mathbf{B}_{u} + \mathbf{B}_{\phi}^{T} \frac{\partial(-\tilde{\mathbf{D}})}{\partial \mathbf{G}} \mathbf{H}_{u} \right\} d\Omega_0 \tag{68}$$

$$\mathbf{K}_{u\phi}(\phi,\mathbf{u}) = \int_{\Omega_0} \mathbf{H}_{u}^{T} \frac{\partial \mathcal{S}}{\partial \nabla \phi} \mathbf{B}_{\phi} d\Omega_0 \tag{69}$$

$$\mathbf{K}_{uu}(\phi,\mathbf{u}) = \int_{\Omega_0} \left\{ \mathbf{B}_{u}^{T} \frac{\partial \tilde{\mathbf{\Sigma}}}{\partial \mathbf{F}} \mathbf{B}_{u} + H_{u}^{T} \frac{\partial \mathcal{S}}{\partial \mathbf{F}} \mathbf{B}_{u} + \mathbf{H}_{u}^{T} \frac{\partial \mathcal{S}}{\partial \mathbf{G}} \mathbf{H}_{u} \right\} d\Omega_0 \tag{70}$$

6. Nonlinear topology optimization formulation for soft dielectrics with flexoelectricity

6.1. Strain Density Function (SDF) interpolation scheme by SIMP method and linear material interpolation model

Topology optimization (TO) consists in finding the optimum distribution of materials in a given structural domain and maximizing specific physical properties. In the SIMP framework used, structural topology can be represented by local material densities, and material properties are interpolated with respect to local density in a continuous manner, with penalty exponents used to force local densities to converge to 1 or 0 (so-called "black-white designs"). Then, the following interpolation scheme is adopted:

$$\begin{aligned}\Psi(\rho) =& [m_{in} + (1-m_{in})\rho^{p_c}](\Psi_{elast} + \Psi_{elast}^{grad}) + [m_{in} + (1-m_{in})\rho^{p_f}]\Psi_{flexo} \\ &+ [m_{in} + (1-m_{in})\rho]\Psi_{diel}\end{aligned} \tag{71}$$

It is worth noting that in the above, the interpolation related to the term Ψ_{diel} is linear. We have observed that this linear term improves the convergence of the topology optimization scheme in the present context. On the other hand, larger values of this exponent are not necessary to define a material density between zero and 1, as this property is provided by the exponents of the other terms.

The electric displacement $\tilde{\mathbf{D}}$ defined in (24) is interpolated as:

$$\tilde{\mathbf{D}}(\rho) = -[\varepsilon_0 + (\varepsilon - \varepsilon_0)\rho] J \mathbf{C}^{-1} \nabla_X \phi - \rho^{p_f} J f (\varepsilon - \varepsilon_0) \mathbf{F}^{-1} G_{ikk} \tag{72}$$

where the small value $m_{in} = 1 \times 10^{-9}$ is employed to mimic the properties of void phase, ε is electric permittivity of solid material, ε_0 is the vacuum electric permittivity, and p_c and p_f are penalty exponents, taken as $p_c = p_f = 3$ in the following numerical examples.

6.2. Energy remedy for void region

To circumvent the numerical instability induced by excessive deformations in low stiffness regions, an energy remedy scheme proposed by Wang[71] is extended to nonlinear electromechanical system. The energy density is interpolated between the nonlinear energy density and the linear energy density. The energy remedy form can be defined as:

$$\widehat{\Psi}(\phi,\mathbf{u}) = \Psi^{NL}(\phi,\theta\mathbf{u}) - \Psi^{L}(\phi,\theta\mathbf{u}) + \Psi^{L}(\phi,\mathbf{u}) \tag{73}$$

where Ψ^{NL} is defined in terms of (5)-(9), and

$$\Psi^{L}(\phi,\mathbf{u}) = \underbrace{\frac{1}{2}\lambda\varepsilon_{kk}^{2} + \mu\varepsilon_{ij}\varepsilon_{ij}}_{linear\ elast} + \underbrace{\frac{1}{2}A_{ij}P_i^L P_j^L}_{dielectric} + \underbrace{\frac{g}{2}G_{ikk}G_{ill} + fP_i^L G_{ikk}}_{flexoelectric} \tag{74}$$

$\lambda = \frac{E\nu}{1-\nu^2}$. By linear form of the first equation in (19), i.e. $\nabla_X\phi + \frac{\partial\Psi^L}{\partial\tilde{\mathbf{P}}^L} = 0$, we obtain the P_i^L as

$$P_i^L = -(\varepsilon-\varepsilon_0)(fG_{ikk} + \nabla_i\phi) \tag{75}$$

then

$$D_i^L = -\varepsilon\nabla_i\phi - f(\varepsilon-\varepsilon_0)G_{ikk} \tag{76}$$

$$\Sigma_{ij}^L = \lambda\varepsilon_{kk}\delta_{ij} + 2\mu\varepsilon_{ij} \tag{77}$$

$$\mathcal{S}_{ijk}^L = gG_{ipp}\delta_{jk} + f\tilde{P}_i^L\delta_{jk} \tag{78}$$

The interpolation parameter $\theta = 1$ for solid region and $\theta = 0$ for void region. It suggests that the stored electromechanical energy corresponds to the non-linear one for solid phase($\theta = 1$) and the linear one for void phase($\theta = 0$). To ensure differentiability, θ in (73) is defined by a smoothed Heaviside projection function,

$$\theta = \frac{\tanh(\beta_1\alpha) + \tanh(\beta_1(\tilde{\rho}-\alpha))}{\tanh(\beta_1\alpha) + \tanh(\beta_1(1-\alpha))} \tag{79}$$

When $\beta_1 \to \infty$, $\theta = 1$ if $\tilde{\rho} > \alpha$, $\theta = 0$ if $\tilde{\rho} < \alpha$. We state that the symbols with subscript 'L' correspond to linear terms, while the symbols with subscript 'NL' correspond to non-linear ones, and the symbols with subscript 'θ' represent the terms where the displacements are interpolated by θ defined in (79).

Using (73), the flexoelectric boundary values problems are given:

$$\begin{cases} \nabla_X \cdot \widehat{\mathbf{D}} = \widehat{\rho}^e \; in \; \Omega_0, \\ \nabla_X \cdot \widehat{\mathbf{\Sigma}} - \nabla_X \cdot (\nabla_X \cdot \widehat{\mathcal{S}}) + \widehat{\mathbf{f}}^e = 0, \; in \; \Omega_0 \end{cases} \tag{80}$$

and

$$\widehat{\mathbf{D}} = \mathbf{D}^{NL,\theta} - \mathbf{D}^{L,\theta} + \mathbf{D}^{L} \tag{81}$$

$$\widehat{\mathbf{\Sigma}} = \mathbf{\Sigma}^{NL,\theta} - \mathbf{\Sigma}^{L,\theta} + \mathbf{\Sigma}^{L} \tag{82}$$

$$\widehat{\mathcal{S}} = \mathcal{S}^{NL,\theta} - \mathcal{S}^{L,\theta} + \mathcal{S}^{L} \tag{83}$$

where $\mathbf{\Sigma}^{NL,\theta}$, $\mathcal{S}^{NL,\theta}$ and $\mathbf{D}^{NL,\theta}$ are respectively defined in (17), (18) and (24) with the displacements $\mathbf{u}$ interpolated by θ. In the above, $\mathbf{D}^{L,\theta}$, $\Sigma^{L,\theta}$ and $\mathcal{S}^{L,\theta}$ are respectively given using (76), (77) and (78) and the displacement interpolation parameter θ.

The residuals are calculated by

$$\begin{cases} \widehat{\mathbf{R}}_\phi(\mathbf{u},\phi) = \widehat{\mathbf{q}}(\mathbf{u},\phi) - \widehat{\mathbf{q}}^{ext} = \mathbf{q}^{NL,\theta}(\mathbf{u},\phi) - \mathbf{q}^{L,\theta}(\mathbf{u},\phi) + \mathbf{q}^{L}(\mathbf{u},\phi) - \widehat{\mathbf{q}}^{ext} = 0 \\ \widehat{\mathbf{R}}_u(\mathbf{u},\phi) = \widehat{\mathbf{f}}(\mathbf{u},\phi) - \widehat{\mathbf{f}}^{ext} = \mathbf{f}^{NL,\theta}(\mathbf{u},\phi) - \mathbf{f}^{L,\theta}(\mathbf{u},\phi) + \mathbf{f}^{L}(\mathbf{u},\phi) - \widehat{\mathbf{f}}^{ext} = 0 \end{cases} \tag{84}$$

where

$$\mathbf{q}^{NL,\theta}(\mathbf{u},\phi) = \mathbf{q}(\theta\mathbf{u},\phi) \tag{85}$$

$$\mathbf{f}^{NL,\theta}(\mathbf{u},\phi) = \mathbf{f}(\theta\mathbf{u},\phi) \tag{86}$$

$$\mathbf{q}^{L}(\mathbf{u},\phi) = \int_{\Omega_0} -\mathbf{D}^L \cdot \nabla_X(\delta\phi) d\Omega_0 \tag{87}$$

$$\mathbf{f}^{L}(\mathbf{u},\phi) = \int_{\Omega_0} \mathbf{\Sigma}^L : \delta\mathbf{u} d\Omega_0 + \int_{\Omega_0} \mathcal{S}^L \vdots \delta\mathbf{G} d\Omega_0 \tag{88}$$

The following discrete system associated with the linearized problem in the Newton algorithm is obtain as:

$$\begin{bmatrix} \widehat{\mathbf{K}}_{\phi\phi}(\phi,\mathbf{u},\theta) & \widehat{\mathbf{K}}_{\phi u}(\phi,\mathbf{u},\theta) \\ \widehat{\mathbf{K}}_{u\phi}(\phi,\mathbf{u},\theta) & \widehat{\mathbf{K}}_{uu}(\phi,\mathbf{u},\theta) \end{bmatrix} \begin{bmatrix} \Delta\phi \\ \Delta\mathbf{u} \end{bmatrix} = - \begin{bmatrix} \widehat{\mathbf{R}}_\phi \\ \widehat{\mathbf{R}}_u \end{bmatrix} \tag{89}$$

where

$$\widehat{\mathbf{K}}_{\phi\phi}(\phi,\mathbf{u},\theta) = \frac{\partial \mathbf{q}^{NL,\theta}}{\partial \phi} - \frac{\partial \mathbf{q}^{L,\theta}}{\partial \phi} + \frac{\partial \mathbf{q}^{L}}{\partial \phi} = \mathbf{K}_{\phi\phi}^{NL,\theta} - \mathbf{K}_{\phi\phi}^{L,\theta} + \mathbf{K}_{\phi\phi}^{L} \tag{90}$$

$$\widehat{\mathbf{K}}_{\phi u}(\phi,\mathbf{u},\theta) = \frac{\partial \mathbf{q}^{NL,\theta}}{\partial \mathbf{u}} - \frac{\partial \mathbf{q}^{L,\theta}}{\partial \mathbf{u}} + \frac{\partial \mathbf{q}^{L}}{\partial \mathbf{u}} = \mathbf{K}_{\phi u}^{NL,\theta} - \mathbf{K}_{\phi u}^{L,\theta} + \mathbf{K}_{\phi u}^{L} \tag{91}$$

$$\widehat{\mathbf{K}}_{u\phi}(\phi,\mathbf{u},\theta) = \frac{\partial \mathbf{f}^{NL,\theta}}{\partial \phi} - \frac{\partial \mathbf{f}^{L,\theta}}{\partial \phi} + \frac{\partial \mathbf{f}^{L}}{\partial \phi} = \mathbf{K}_{u\phi}^{NL,\theta} - \mathbf{K}_{u\phi}^{L,\theta} + \mathbf{K}_{u\phi}^{L} \tag{92}$$

$$\widehat{\mathbf{K}}_{uu}(\phi,\mathbf{u},\theta) = \frac{\partial \mathbf{f}^{NL,\theta}}{\partial \mathbf{u}} - \frac{\partial \mathbf{f}^{L,\theta}}{\partial \mathbf{u}} + \frac{\partial \mathbf{f}^{L}}{\partial \mathbf{u}} = \mathbf{K}_{uu}^{NL,\theta} - \mathbf{K}_{uu}^{L,\theta} + \mathbf{K}_{uu}^{L} \tag{93}$$

$$\mathbf{K}_{\phi\phi}^{NL,\theta} = \int_{\Omega_0} B_\phi^T \frac{\partial(-\tilde{D}_i^{NL,\theta})}{\partial \nabla_m \phi} B_\phi \, d\Omega_0 \tag{94}$$

$$\mathbf{K}_{\phi u}^{NL,\theta} = \int_{\Omega_0} \left\{ B_\phi^T \frac{\partial(-\tilde{D}_i^{NL,\theta})}{\partial F_{kl}} B_u + B_\phi^T \frac{\partial(-\tilde{D}_i^{NL,\theta})}{\partial G_{jkl}} H_u \right\} \theta \, d\Omega_0 \tag{95}$$

$$\mathbf{K}_{u\phi}^{NL,\theta} = \int_{\Omega_0} H_u^T \frac{\partial \mathcal{S}_{ijk}^{NL,\theta}}{\partial \nabla_l \phi} B_\phi \, d\Omega_0 \tag{96}$$

$$\mathbf{K}_{uu}^{NL,\theta} = \int_{\Omega_0} \left\{ B_u^T \frac{\partial \tilde{\Sigma}_{ij}^{NL,\theta}}{\partial F_{kl}} B_u + H_u^T \frac{\partial \mathcal{S}_{ijk}^{NL,\theta}}{\partial F_{lm}} B_u + H_u^T \frac{\partial \mathcal{S}_{ijk}^{NL,\theta}}{\partial G_{lmn}} H_u \right\} \theta \, d\Omega_0 \tag{97}$$

$$\mathbf{K}_{\phi\phi}^{L} = \mathbf{K}_{\phi\phi}^{L,\theta} = \int_{\Omega_0} B_\phi^T \varepsilon \delta_{ij} B_\phi \, d\Omega_0 \tag{98}$$

$$\mathbf{K}_{u\phi}^{L} = \mathbf{K}_{u\phi}^{L,\theta} = -\int_{\Omega_0} H_u^T f(\varepsilon - \varepsilon_0) \delta_{il} \delta_{jk} B_\phi \, d\Omega_0 \tag{99}$$

$$\mathbf{K}_{\phi u}^{L} = \int_{\Omega_0} B_\phi^T f(\varepsilon - \varepsilon_0) \delta_{ij} \delta_{kl} H_u \, d\Omega_0 \tag{100}$$

$$\mathbf{K}_{uu}^{L} = \int_{\Omega_0} \left\{ B_u^T [\lambda \delta_{ij} \delta_{kl} + \mu(\delta_{ik}\delta_{jl} + \delta_{il}\delta_{jk})] B_u + H_u^T [g - f^2(\varepsilon - \varepsilon_0)] \delta_{il} \delta_{mn} \delta_{jk} H_u \right\} d\Omega_0 \tag{101}$$

$$\mathbf{K}_{\phi u}^{L,\theta} = \int_{\Omega_0} B_\phi^T f(\varepsilon - \varepsilon_0) \delta_{ij} \delta_{kl} H_u \theta \, d\Omega_0 \tag{102}$$

$$\mathbf{K}_{uu}^{L,\theta} = \int_{\Omega_0} \left\{ B_u^T [\lambda \delta_{ij} \delta_{kl} + \mu(\delta_{ik}\delta_{jl} + \delta_{il}\delta_{jk})] B_u + H_u^T [g - f^2(\varepsilon - \varepsilon_0)] \delta_{il} \delta_{mn} \delta_{jk} H_u \right\} \theta \, d\Omega_0 \tag{103}$$

After solving the linearized equation (89), the nodal electric potentials and displacements are updated through

$$\begin{aligned}\phi^{k+1} &= \phi^{k}+\Delta\phi\\ \mathbf{u}^{k+1} &= \mathbf{u}^{k}+\Delta\mathbf{u}\end{aligned} \tag{104}$$

until a convergence criterion is reached. The algorithm for solving the nonlinear problem (84) is illustrated in Algorithm.1. It is important to note that the equations for the optimization model are calculated using the final converged state variables of the structural equilibrium residual vectors defined in (84).

Algorithm 1 The algorithm for nonlinear problem (84)

```
Initialize: $[\mathbf{u}^{(0)};\phi^{(0)}]=\mathbf{0}$, $tol=10^{-8}$;
for $n=1$ to $N$ (Loop over all load increments) do
    Initialize: $err=1$, $k=0$;
    $\mathbf{u}^{(k,n)}=\mathbf{u}^{(n-1)}$, $\phi^{(k,n)}=\phi^{(n-1)}$;
    while $err>tol$ do
        Compute tangent stiffness $\widehat{\mathbf{K}}_{tan}(\phi^{(k,n)},\mathbf{u}^{(k,n)})$ from (90)-(103);
        Compute residual $\widehat{\mathbf{R}}(\phi^{(k,n)},\mathbf{u}^{(k,n)})$ from (84);
        Compute $\Delta\mathbf{u}^{(k,n)}$ and $\Delta\phi^{(k,n)}$ from (89);
        Update $\mathbf{u}^{(k+1,n)}=\mathbf{u}^{(k,n)}+\Delta\mathbf{u}^{(k,n)}$, $\phi^{(k+1,n)}=\phi^{(k,n)}+\Delta\phi^{(k,n)}$;
        $err=\|\widehat{\mathbf{R}}^{(k,n)}\|$;
        $k=k+1$;
    end while
    $\mathbf{u}^{(n)}=\mathbf{u}^{(k,n)}$, $\phi^{(n)}=\phi^{(k,n)}$;
end for
return $\mathbf{u}=\mathbf{u}^{(k,N)}$, $\phi=\phi^{(k,N)}$;
```

6.3. Optimization problem formulation

Here we formulate the topology optimization problem to maximize the electromechanical coupling factor (ECF) of non-linear flexoelectric structures:

$$\begin{aligned}&\text{Minimize}: \quad J=\frac{1}{k_{eff}^{2}}=\frac{\Pi_m}{\Pi_e}\\ &\text{Subject to}: \quad \begin{cases}\frac{1}{|\Omega|}\int_{\Omega}\bar{\rho}\,d\Omega-v_f\leq 0\\ \widehat{\mathbf{R}}(\phi,\mathbf{u})=0\\ \hat{C}(\rho)\leq\hat{C}^{max}\\ 0\leq\rho_e\leq 1,\end{cases}\end{aligned} \tag{105}$$

where

$$\Pi_m = (\widehat{\mathbf{f}}^{ext})^T \mathbf{u} \tag{106}$$

$$\Pi_e = \frac{1}{2}\phi^T \widehat{\mathbf{K}}_{\phi\phi}\phi \tag{107}$$

and $\widehat{\mathbf{R}}(\phi,\mathbf{u}) = [\widehat{\mathbf{R}}_\phi;\ \widehat{\mathbf{R}}_u]$ is the residual vector of the structural equilibrium defined by (84). $\hat{C}(\rho) = \Pi_m$ is the average compliance of the structure, which it is expected to eliminate disconnected domain by ensuring a minimal stiffness to the structure.

The continuous density design variable ρ in the optimization formulation (105) yields a ill-posed problem, inducing checkerboards and mesh-dependence. In order to enforce its well-posedness (smoothness and mesh-independence), a projection filter [49, 74] is defined by a convolution of the density ρ with a non-negative smooth kernel $h(\boldsymbol{x},\bar{\boldsymbol{x}})$, such that ρ can inherit the smoothness characteristics of the kernel.

$$\bar{\rho}(\boldsymbol{x}) = \int_\Omega h(\boldsymbol{x},\bar{\boldsymbol{x}})\rho(\bar{\boldsymbol{x}})d\bar{\boldsymbol{x}}, \qquad \int_\Omega h(\boldsymbol{x},\bar{\boldsymbol{x}})d\bar{\boldsymbol{x}} = 1 \tag{108}$$

The discretization of projection in (108) can be expressed as:

$$\bar{\rho}_j = \sum_{\bar{i}=1}^{n_s} \psi(\rho_{\bar{i}})\rho_{\bar{i}} = \frac{\sum_{\bar{i}=1}^{n_s} w(r_{\bar{i}})\rho_{\bar{i}}}{\sum_{\hat{i}=1}^{n_s} w(r_{\hat{i}})} \tag{109}$$

where the weight function $w(r)$ can be defined as a compactly supported radial basis functions (RBFs) with higher-order continuity and non-negativity[75]:

$$w(r) = (1-r)_+^6 \cdot (35r^2 + 18r + 3), \qquad r = d/r_{min} \tag{110}$$

where the symbol $(1-r)_+ = max(0, 1-r)$. d is the Euclidean distances between the current nodal density and the neighborhood nodal density lying within the local support domain, and r_{min} denotes the radius of the local support domain.

A smoothed Heaviside projection is used to map the intermediate density to 1 or 0 by a prescribed threshold value. It is defined as:

$$\tilde{\rho} = \frac{\tanh(\beta\rho_0) + \tanh(\beta(\bar{\rho} - \rho_0))}{\tanh(\beta\rho_0) + \tanh(\beta(1-\rho_0))} \tag{111}$$

where β controls the sharpness of the projection, and ρ_0 is the threshold value.

6.4. Sensitivity analysis

The adjoint method is employed to derive the sensitivity of electromechanical coupling factor with respect to local densities $\tilde{\rho}$:

$$\frac{dJ}{d\tilde{\rho}} = \frac{1}{\Pi_e^2}(\frac{d\Pi_m}{d\tilde{\rho}}\Pi_e - \Pi_m\frac{d\Pi_e}{d\tilde{\rho}}) \tag{112}$$

We construct the Lagrangian equations for mechanical and electric energy, respectively as:

$$\Pi_m = \Pi_m - \boldsymbol{\lambda}^T\hat{\mathbf{R}} \tag{113}$$

$$\Pi_e = \Pi_e - \boldsymbol{\mu}^T\widehat{\mathbf{R}} \tag{114}$$

As the residual vector $\widehat{\mathbf{R}} = 0$ holds, the adjoint vectors $\boldsymbol{\lambda}$ and $\boldsymbol{\mu}$ are arbitrary vectors.

The derivatives of the Lagrangian equations with respect to density can be obtained as:

$$\begin{aligned}\frac{d\Pi_m}{d\tilde{\rho}} =& \frac{\partial\Pi_m}{\partial\tilde{\rho}} + \frac{\partial\Pi_m}{\partial\mathbf{Z}}\cdot\frac{\partial\mathbf{Z}}{\partial\tilde{\rho}} - \boldsymbol{\lambda}^T(\frac{\partial\widehat{\mathbf{R}}}{\partial\tilde{\rho}} + \frac{\partial\widehat{\mathbf{R}}}{\partial\theta}\cdot\frac{\partial\theta}{\partial\tilde{\rho}} + \frac{\partial\widehat{\mathbf{R}}}{\partial\mathbf{Z}}\cdot\frac{\partial\mathbf{Z}}{\partial\tilde{\rho}})\\ =& -\boldsymbol{\lambda}^T(\frac{\partial\widehat{\mathbf{R}}}{\partial\tilde{\rho}} + \frac{\partial\widehat{\mathbf{R}}}{\partial\theta}\cdot\frac{\partial\theta}{\partial\tilde{\rho}}) + (\mathbf{f}^T - \boldsymbol{\lambda}^T\frac{\partial\widehat{\mathbf{R}}}{\partial\mathbf{Z}})\frac{\partial\mathbf{Z}}{\partial\tilde{\rho}}\end{aligned} \tag{115}$$

$$\begin{aligned}\frac{d\Pi_e}{d\tilde{\rho}} =& \frac{\partial\Pi_e}{\partial\tilde{\rho}} + \frac{\partial\Pi_e}{\partial\mathbf{Z}}\cdot\frac{\partial\mathbf{Z}}{\partial\tilde{\rho}} - \boldsymbol{\mu}^T(\frac{\partial\widehat{\mathbf{R}}}{\partial\tilde{\rho}} + \frac{\partial\widehat{\mathbf{R}}}{\partial\theta}\cdot\frac{\partial\theta}{\partial\tilde{\rho}} + \frac{\partial\widehat{\mathbf{R}}}{\partial\mathbf{Z}}\cdot\frac{\partial\mathbf{Z}}{\partial\tilde{\rho}})\\ =& \frac{1}{2}\boldsymbol{\phi}^T\frac{\partial\widehat{\mathbf{K}}_{\phi\phi}}{\partial\tilde{\rho}}\boldsymbol{\phi} - \boldsymbol{\mu}^T(\frac{\partial\widehat{\mathbf{R}}}{\partial\tilde{\rho}} + \frac{\partial\widehat{\mathbf{R}}}{\partial\theta}\cdot\frac{\partial\theta}{\partial\tilde{\rho}})\\ &+ \left\{\left[\boldsymbol{\phi}^T\widehat{\mathbf{K}}_{\phi\phi},\ \frac{1}{2}\boldsymbol{\phi}^T\frac{\partial\widehat{\mathbf{K}}_{\phi\phi}(\mathbf{u})}{\partial\mathbf{u}}\boldsymbol{\phi}\right] - \boldsymbol{\mu}^T\frac{\partial\widehat{\mathbf{R}}}{\partial\mathbf{Z}}\right\}\frac{\partial\mathbf{Z}}{\partial\tilde{\rho}}\end{aligned} \tag{116}$$

where $\mathbf{Z} = [\boldsymbol{\phi};\mathbf{u}]$ and

$$\frac{\partial\widehat{\mathbf{R}}}{\partial\mathbf{Z}} = \begin{bmatrix} \widehat{\mathbf{K}}_{\phi\phi} & \widehat{\mathbf{K}}_{\phi u} \\ \widehat{\mathbf{K}}_{u\phi} & \widehat{\mathbf{K}}_{uu} \end{bmatrix} \tag{117}$$

$$\frac{\partial\widehat{\mathbf{R}}}{\partial\theta} = \begin{bmatrix} \mathbf{K}_{\phi u}^{NL,\theta} - \mathbf{K}_{\phi u}^{L,\theta} \\ \mathbf{K}_{uu}^{NL,\theta} - \mathbf{K}_{uu}^{L,\theta} \end{bmatrix}\mathbf{u} \tag{118}$$

The adjoint vectors can be calculated by the following adjoint equations, in order to eliminate the implicit term $\frac{\partial \mathbf{Z}}{\partial \tilde{\rho}}$ in (115) and (116):

$$\boldsymbol{\lambda}^T \frac{\partial \widehat{\mathbf{R}}}{\partial \mathbf{Z}} = \mathbf{f}^T \tag{119}$$

$$\boldsymbol{\mu}^T \frac{\partial \widehat{\mathbf{R}}}{\partial \mathbf{Z}} = \left[\phi^T \widehat{\mathbf{K}}_{\phi\phi},\ \frac{1}{2}\phi^T \frac{\partial \mathbf{K}_{\phi\phi}^{NL,\theta}(\mathbf{u})}{\partial \mathbf{u}} \phi \right] \tag{120}$$

where

$$\frac{\partial \mathbf{K}_{\phi\phi}^{NL,\theta}(\mathbf{u})}{\partial \mathbf{u}} = \int_{\Omega_0} B_\phi^T \frac{\partial^2(-\tilde{D}_i^{NL,\theta})}{\partial(\nabla_j \phi)\partial u_k} B_\phi d\Omega_0 \tag{121}$$

and

$$\frac{\partial^2(-\tilde{D}_i^{NL,\theta})}{\partial(\nabla_j \phi)\partial u_k} = J\varepsilon\theta(C_{ij}^{-1}F_{lk}^{-1} - F_{ik}^{-1}C_{jl}^{-1} - C_{il}^{-1}F_{jk}^{-1})\nabla_l \tag{122}$$

7. Numerical examples

7.1. Bending cantilever beam

In this first example, we consider a cantilever beam subjected to bending deformation, as shown in Fig.2. The left end is fixed and the bottom is grounded, while the force is imposed on the top-right point. The dimension of the beam is $h_1 \times L_1 = 0.2\mu m \times 0.8\mu m$. The material of the beam is polyvinylidene fluoride (PVDF), which is a widely studied polymer in soft dielectrics and nonlinear flexoelectricity[10, 28, 43, 68]. Its parameters are[10]: Young's modulus $E = 3.7$ GPa, Poisson's ratio $\nu = 0.3$, dielectric permittivity $\varepsilon = 9.2\varepsilon_0$, flexoelectric coefficient $f = 179$ V. Here, the couple strain constant is taken as $g = 4 \times 10^{-6}$ N. The vacuum electric permittivity is $\varepsilon_0 = 8.854 \times 10^{-12}$ F/m. The isotropic material assumption is taken account. The IGA discretization for beam is 124×31 control points. The variation of electromechanical coupling factors (ECFs) for bending cantilever beam with respect to the mesh refinement is analyzed in Fig.3. We can note a tendency to convergence, even though this one is quite slow, in view of the low difference between the initial and final values.

The topology optimization of the cantilever beam is performed under the force F_1=-0.1 N, F_1=-1 N, F_1=-2 N, F_1=-2.5 N and F_1=-3 N, respectively. The volume fraction constraint, defined as the quantity of material as compared to the design

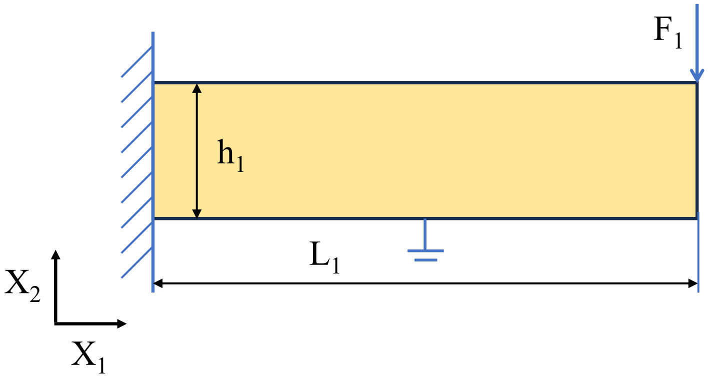

Figure 2: Bending beam-like soft dielectrics with open circuit boundary conditions: design domain

domain volume $h_1 \times L_1$ is set as v_f =0.6 for all load cases. The parameters of Heaviside projection function (79) in energy remedy formulation are chosen as $\alpha = 0.1$ and $\beta_1 = 500$. The compliance constraint in (105) is set to $\hat{C}^{max} = 4\overline{\Pi}_1$, where $\overline{\Pi}_1$ is the strain energy of the undesigned flexoelectric beam, i.e. the beam with all the relative densities $\rho = 1$. For comparison, a guess design consisting into a rectangular beam with 4 holes as depicted in Fig.4(a) is analyzed. The holes radii are $R = 0.3568h_1$ corresponding to a volume fraction equal to 0.6. This structure will serve as a reference to be compared with the optimized designs. The penalty exponents used in the TO numerical procedure (see Eqs.(71)-(72)) are chosen here as $p_c = p_f = 3$.

We carry out the optimization of the cantilever beam, where the initialization of the densities is performed by setting them uniformly to $\rho_i = 0.6$, $(i = 1, ..., N_{cp})$ in the rectangular design domain defined in Fig. 2. N_{cp} denotes the number of control points in IGA. At the initial stage of optimization, uniform structural densities lead to a significant degradation in the overall mechanical strength of the material, making it prone to excessive deformation and unable to be optimized as the force increases. To address this issue, a heuristic continuation scheme is implemented on the mechanical penalty factor p_c. In this study, the updating scheme for the mechanical penalty factor p_c is set as $p_c = min(p_c + \Delta p, 3)$ every 3 steps

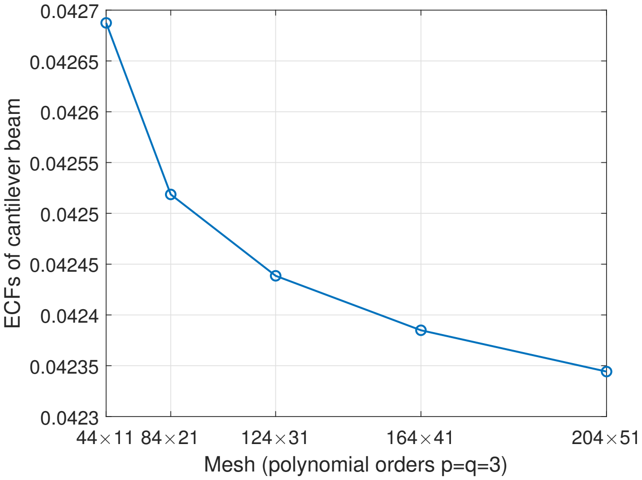

Figure 3: Electromechanical coupling factors (ECFs) for bending cantilever beam with respect to the mesh refinement

after the iteration has exceeded 10, with $\Delta p = 0.1$ and initial $p_c = 1$. The final optimized geometries, obtained respectively for the force magnitudes F_1=-0.1 N, F_1=-1 N, F_1=-2 N, F_1=-2.5 N and F_1=-3 N, are depicted in Fig.4. Observing the topology figures, we can see that the optimum structures contain no holes and that the distribution of materials is more concentrated. Different initializations have been tested: uniform densities and circular voids. Numerical investigations, not shown here, have concluded that they both converged to the same topology. The optimization of electromechanical coupling factors (ECFs) for different forces is given in Fig.5. All the iteration curves show that the optimization process is stable. The corresponding electromechanical coupling factors (ECFs) are listed in Table 1. The ECFs of the optimized structures for forces F_1=-0.1 N, F_1=-1 N, F_1=-2 N, F_1=-2.5 N and F_1=-3 N increase by factors of 9.2638, 9.4201, 9.1106, 8.9157 and 8.7066 times, respectively, as compared to the reference design in Fig.4(a). It can be seen that in the present example, the optimal electromechanical coupling factors first increase slightly, then decrease significantly as the external forces applied for optimization increase.

The distribution of electric potentials and deformed configurations for optimal structures under different forces is illustrated in Fig.6. We can see that the optimized structure produces very large deformations under the increased loads. In particular, the potential in the upper left part of the beam is more pronounced. Furthermore, it can be clearly seen that the amplitudes of the electrical potentials

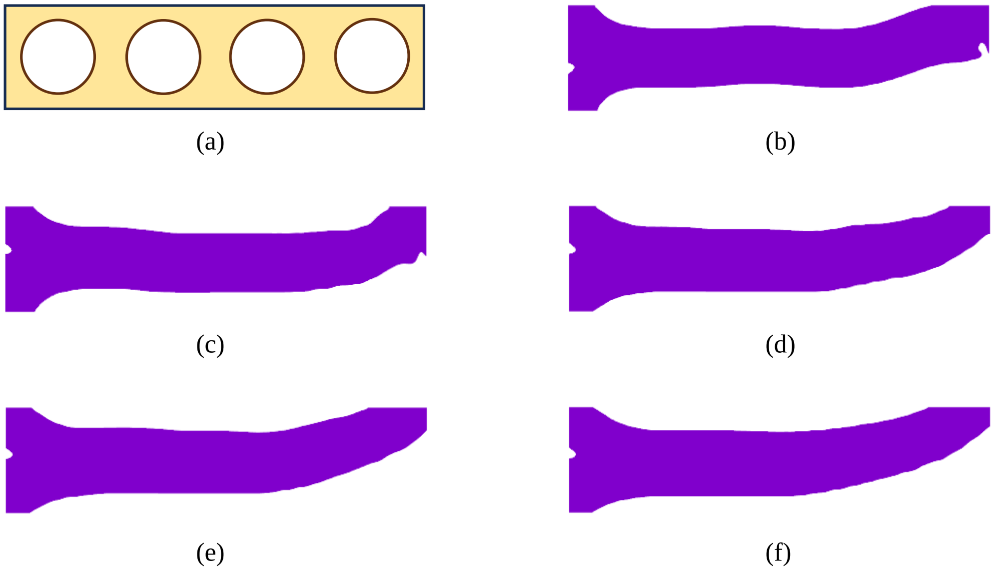
(a) (b) (c) (d) (e) (f)

Figure 4: Reference structure and optimized designs for beam-like soft dielectrics by different loads, with beam size $h_1 \times L_1 = 0.2\mu m \times 0.8\mu m$: (a) reference structure; (b) optimal design by load $F_1 = -0.1$N; (c) optimal design by load $F_1 = -1$N; (d) optimal design by load $F_1 = -2$N; (e) optimal design by load $F_1 = -2.5$N; (f) optimal design by load $F_1 = -3$N

increase with increasing loading.

The influence of size effect on the topology optimization of nonlinear soft dielectrics under large deformation is also examined in the context of a flexoelectric cantilever beam. We perform the optimization for the flexoelectric beam under the same boundary conditions, but the dimension of the beam is changed as $h_1 \times L_1 = 1\mu m \times 4\mu m$. The optimal designs achieved by forces $F_1 = -3$N and $F_1 = -5$N are depicted in Fig.7. There are some holes in the optimal topology, and they present a significant geometric difference from the optimal structures of beam with size $h_1 \times L_1 = 0.2\mu m \times 0.8\mu m$. The electromechanical coupling factors (ECFs) of optimal structures by the forces $F_1 = -3$N and $F_1 = -5$N are obtained as 0.04641 and 0.04887, respectively. Compared to the previously mentioned smaller-sized beam, the ECFs are smaller for this larger-sized beam, which shows size effect of the optimization for flexoelectric energy harvesters.

The distribution of electric potentials and deformed configuration for optimal

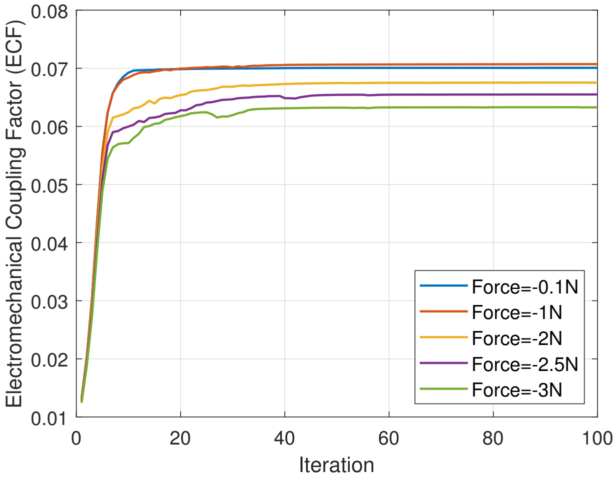

Figure 5: Iteration process of Electromechanical coupling factors (ECF) for bending beam-like soft dielectrics under different loads

Table 1: Electromechanical coupling factors (ECF) of optimal designs for flexible nanobeams under different loads

Force	ECF (optimized)	ECF (reference)	Gain: ECF$_{opt}$/ECF$_{ref}$
-0.1 N	0.07007	6.8272×10^{-3}	10.2638
-1 N	0.07072	6.7865×10^{-3}	10.4201
-2 N	0.06754	6.6801×10^{-3}	10.1106
-2.5 N	0.06550	6.6056×10^{-3}	9.9157
-3 N	0.06329	6.5200×10^{-3}	9.7066

structures of beam with size $h_1 \times L_1 = 1\mu m \times 4\mu m$ is illustrated in Fig.8. We observe that the magnitudes of electric potential for both sizes of beams are similar when the prescribed loads are the same. A beam with a smaller size can produce deformations that are significantly larger in magnitude compared to the structural dimensions. However, in flexoelectricity, the size effect plays a beneficial role in enhancing the electromechanical response. Striking a balance between both the effects is essential for optimal performance. Soft materials capable of large deformations can serve as a bridge in achieving this equilibrium. Larger deformations contribute to the enhancement of electromechanical coupling factors. Consequently, the improvement in electromechanical coupling factors for optimized

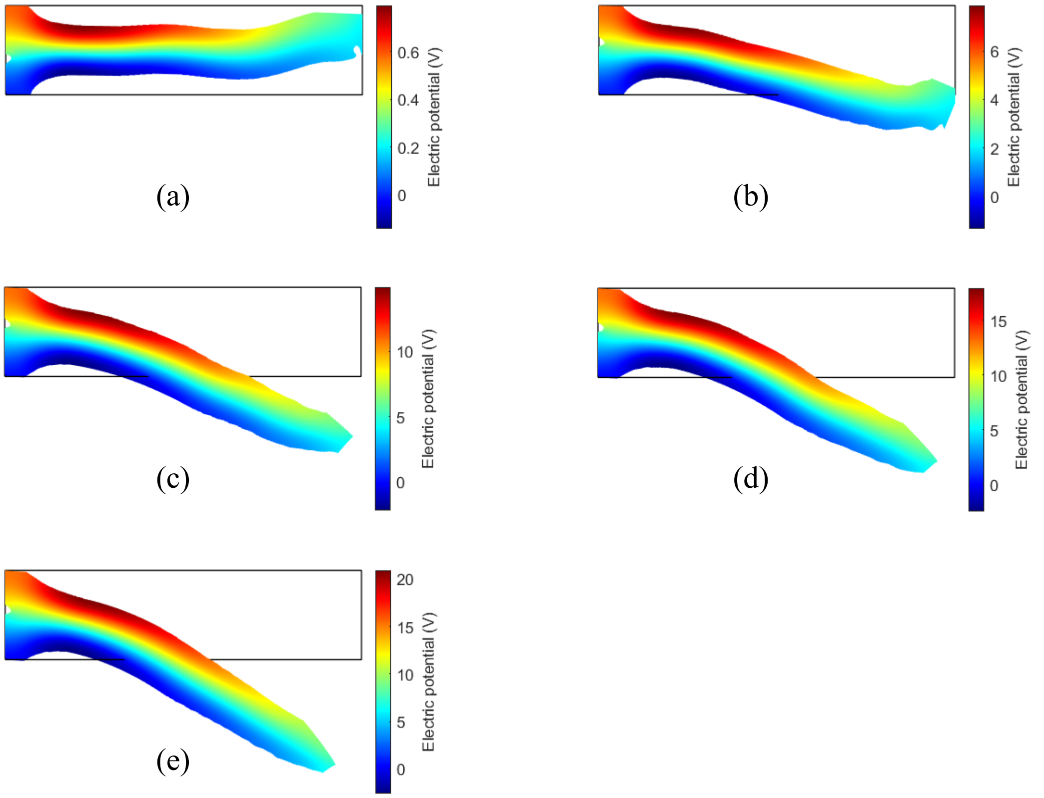
(a) (b) (c) (d) (e)

Figure 6: Distribution of electric potentials and deformed configuration for optimal structures of flexoelectric nano beam under different forces, with beam size $h_1 \times L_1 = 0.2\mu m \times 0.8\mu m$: (a) optimal design by load $F_1 = -0.1$N; (b) optimal design by load $F_1 = -1$N; (c) optimal design by load $F_1 = -2$N; (d) optimal design by load $F_1 = -2.5$N; (e) optimal design by load $F_1 = -3$N

structures stems from the interaction of size effects and large deformations.

7.2. Bending double-clamped beam

In this example, a double-clamped beam undergoing bending deformation is investigated, as illustrated in Fig.9. The dimensions of the beam are $h_2 \times L_2 = 2\mu m \times 8\mu m$. Both ends are fixed, the load is imposed in the middle three points while the bottom surface is connected to the ground. The material is the same as in the previous example, i.e. PVDF. The volume fraction constraint is here set as $f_2 = 0.6$. The compliance constraint in (105) is set as $\hat{C}^{max} = 4\overline{\Pi}_2$, where $\overline{\Pi}_2$ is the strain energy of the double-clamped beam design domain with all $\rho = 1$. The parameters for energy remedy formulation are set as $\alpha = 0.2$ and $\beta_1 = 500$. It is


(a) (b)

Figure 7: Optimal designs of flexoelectric nano beam with size $h_1 \times L_1 = 1\mu m \times 4\mu m$, optimized by different loads: (a) optimal design by load $F_1 = -3$N; (c) optimal design by load $F_1 = -5$N

worthwhile noted that an increase in α to 0.2 enhances the load-carrying capacity of control points characterized by weak densities, thereby enabling optimization under larger deformations without excessive distortion. A reference guess design is outlined in Fig.10(a), comprising a double-clamped beam with four circular voids each having a radius $R = 0.3568h_2$, equivalent to a volume fraction of 0.6. The penalty exponents for the SDF interpolation scheme in Eqs.(71)-(72) are also chosen as $p_c = p_f = 3$.

The topology optimization of the double-clamped beam is performed under the forces values F_2=-1 N, F_2=-10 N, F_2=-20 N, F_2=-25 N, F_2=-30 N and F_2=-35 N, respectively. As an initial step in the optimization algorithm, the design variables values are uniformly set to $\rho_i = 0.6$ $(i = 1, ..., N_{cp})$. The same continuation scheme of the mechanical penalty factor p_c is utilized. The final optimal designs obtained by the forces F_2=-1 N, F_1=-10 N, F_2=-20 N, F_2=-25 N, F_2=-30 N and F_2=-35 N, respectively, are presented in Fig.10. We can observe the variation of topology, where the holes in the optimal designs decreases in size, and the rods at the bottom-left and right become thinner as the force increases. The electrome-

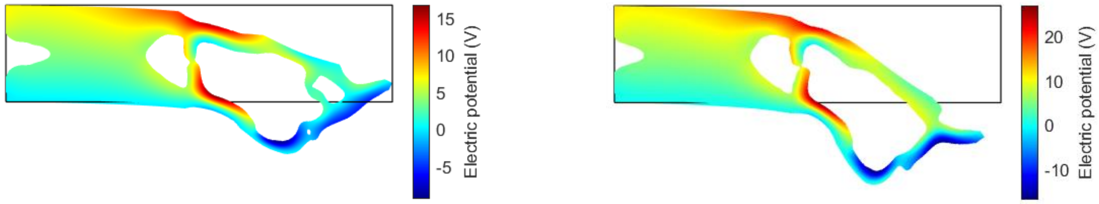

(a) (b)

Figure 8: Distribution of electric potentials and deformed configuration for optimal structures of flexoelectric nano beam with dimension $h_1 \times L_1 = 1\mu m \times 4\mu m$, under different forces: (a) optimal design by load $F_1 = -3$N; (c) optimal design by load $F_1 = -4$N

chanical coupling factors (ECFs) of optimal structures under different forces are presented in Table.2. Notably, the ECFs of the reference structure in Fig.10(a) increase with the increase of force magnitude. Specifically, for the forces F_2=-1 N, F_2=-10 N, F_2=-20 N, F_2=-25 N, F_2=-30 N, and F_2=-35 N, the ECFs improve by factors of 0.6806 1.0630, 1.6878, 1.9005, 2.0496, and 2.2166, respectively, compared to the reference design. The gain in ECFs raises with the increase in force, illustrating here again the nonlinear effects, and in particular the impact of the finite strains on the ECFs gains.

Table 2: Electromechanical coupling factors (ECF) of optimal designs for flexoelectric double-clamped beam under different loads

Force	ECF (optimized)	ECF (reference)	Gain: $\text{ECF}_{opt}/\text{ECF}_{ref}$
-1 N	0.02420	0.01441	1.6806
-10 N	0.02820	0.01367	2.0630
-20 N	0.03278	0.01220	2.6878
-25 N	0.03325	0.01146	2.9005
-30 N	0.03290	0.01079	3.0496
-35 N	0.03274	0.01018	3.2166

The distribution of electric potentials and deformed configuration are illustrated for optimal structures of flexoelectric double-clamped beam obtained by

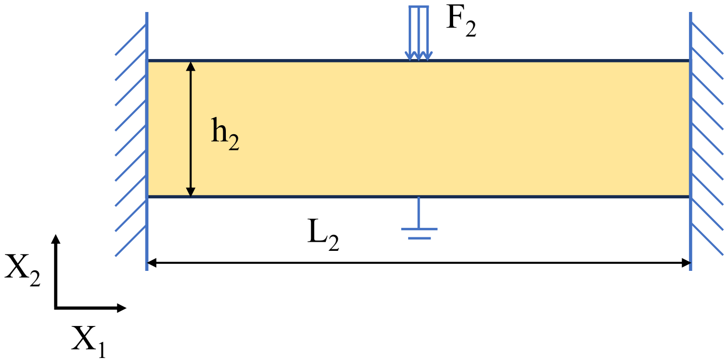

Figure 9: Bending double-clamped beam-like soft dielectrics with open circuit boundary conditions: design domain

different forces in Fig.11. We can see that the local large deformation or strain occurs, due to the concentration force imposed on the top-mid area. The localized nature of the strain typically gives rise to substantial deformations and significant strain gradients occurring within the specific region. It also results in the concentrated distribution of large electric potentials. Similarly, an increase in the force applied on optimization will elevate the amplitude of the distributed electric potentials.

To further investigate the mechanism behind the improvement in the electromechanical coupling factors (ECFs) of the flexoelectric double-clamped beam, we depict the variation of ECFs for the optimized structures in relation to the volume fraction. This analysis is conducted for the case of the force $F_2 = -10$N, as shown in Fig.12, where the topology configuration, distribution of electric potentials and deformations are illustrated. We observe an increase in the ECFs for the optimized structures of the flexoelectric double-clamped beam as the volume fraction rises. Significant local deformation and electric potential are concentrated near the load sites. When the volume fraction is minimal, the support configuration near the loading site on the optimized structure takes on a triangular shape, leading to challenges in generating large deformations at that specific site. As the volume fraction increases, the hole of support structure adjacent to the loading

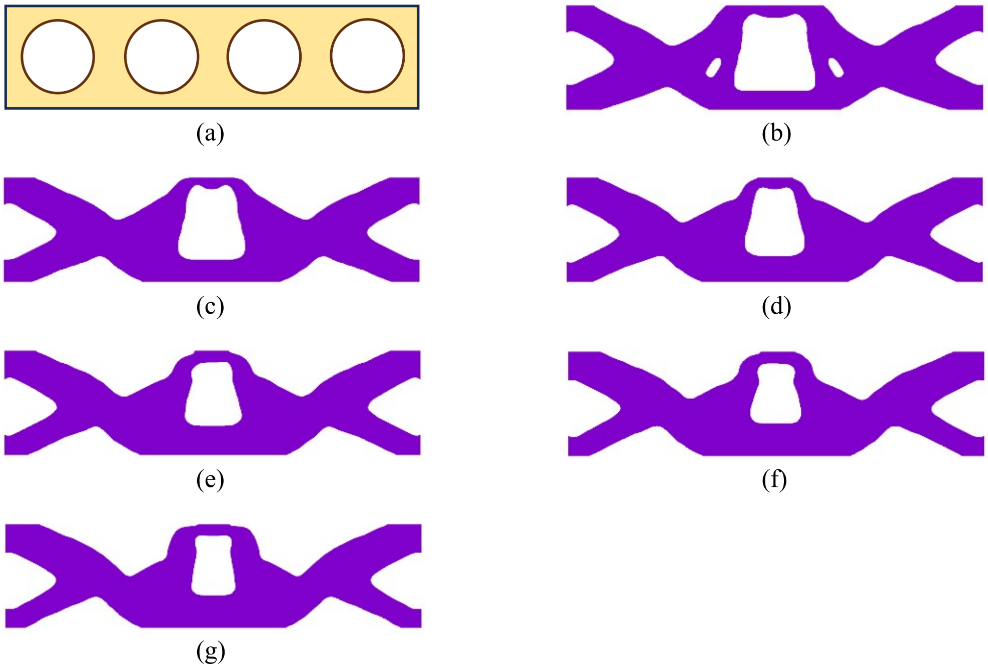

(a) (b) (c) (d) (e) (f) (g)

Figure 10: Reference structure and optimized designs for flexoelectric double-clamped beam under different forces: (a) reference structure; (b) optimal design by load $F_2 = -1\text{N}$; (c) optimal design by load $F_2 = -10\text{N}$; (d) optimal design by load $F_2 = -20\text{N}$; (e) optimal design by load $F_2 = -25\text{N}$; (f) optimal design by load $F_2 = -30\text{N}$; (g) optimal design by load $F_2 = -35\text{N}$

site approximates a polygonal shape (quadrilateral or hexagonal), facilitating the generation of substantial local deformations.

7.3. Compressed truncated pyramid

In this example, a truncated pyramid-like soft dielectrics is considered, as shown in Fig.13. This particular shape is frequently selected in flexoelectric systems to induce strain gradient in compression [76]. The size of the truncated pyramid is $h_1 = 2\mu m$, $a_1 = 2\mu m$ and $a_2 = 6\mu m$. A spatially uniform pressure is applied on the top surface along the X_2-direction and the displacement DOFs on the bottom surface are fixed. The material parameters of PVDF are also employed here. The volume fraction constraint is set as $f_3 = 0.7$. The compliance constraint defined in (105) is here chosen as $\hat{C}^{max} = 3\overline{\Pi}_3$, where $\overline{\Pi}_3$ is the strain energy of the truncated pyramid design domain with all $\rho = 1$. The parameters for energy remedy formulation in (73) are set as $\alpha = 0.2$ and $\beta_1 = 500$. A reference guess design is depicted in Fig.13(a), representing a truncated pyramid with semi-circular

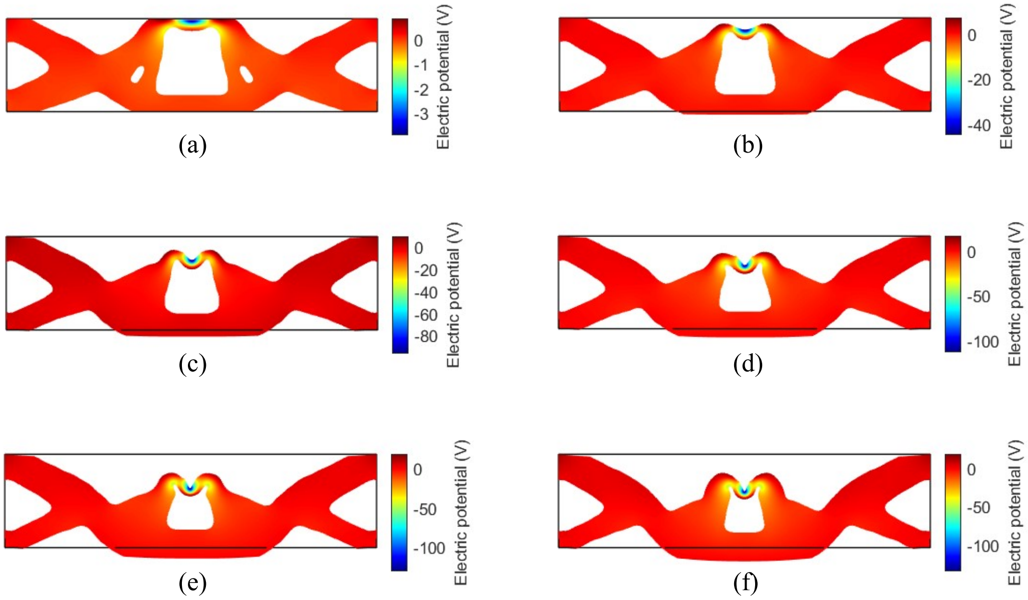

(a) (b)

(c) (d)

(e) (f)

Figure 11: Distribution of electric potentials and deformed configuration for optimal structures of flexoelectric double-clamped beam under different forces: (a) optimal design by load $F_2 = -1$N; (b) optimal design by load $F_2 = -10$N; (c) optimal design by load $F_2 = -20$N; (d) optimal design by load $F_2 = -25$N; (e) optimal design by load $F_2 = -30$N; (f) optimal design by load $F_2 = -35$N

voids on the bottom surface, with a radius $R = 0.6180h_3$, corresponding to a volume fraction of 0.7. The penalty exponents for the SDF interpolation scheme in Eqs.(71)-(72) are set as $p_c = p_f = 3$.

The topology optimization of the truncated pyramid-like soft dielectrics is performed under the forces values F_3=-0.5 N, F_3=-1 N, F_3=-2 N and F_3=-2.5 N, respectively. As an initial step in the optimization algorithm, the design variables are uniformly assigned values of $\rho_i = 0.7$ $(i = 1,...,N_{cp})$. The same continuation scheme of the mechanical penalty factor p_c is also utilized here. The final optimal designs obtained by the forces F_3=-0.5 N, F_3=-1 N, F_3=-2 N and F_3=-2.5 N, respectively, are presented in Fig.14. It is observed that the height and area of the holes in the optimal designs decreases as the force increases. The electromechanical coupling factors (ECFs) of optimal structures under different forces are summarized in Table.3. In this example, the ECFs of the reference structure in Fig.14(a) decrease when the magnitude of the force increases. The ECFs of the optimized structures increase by factors of 6.3446, 6.0646, 6.1426 and 4.7234 for

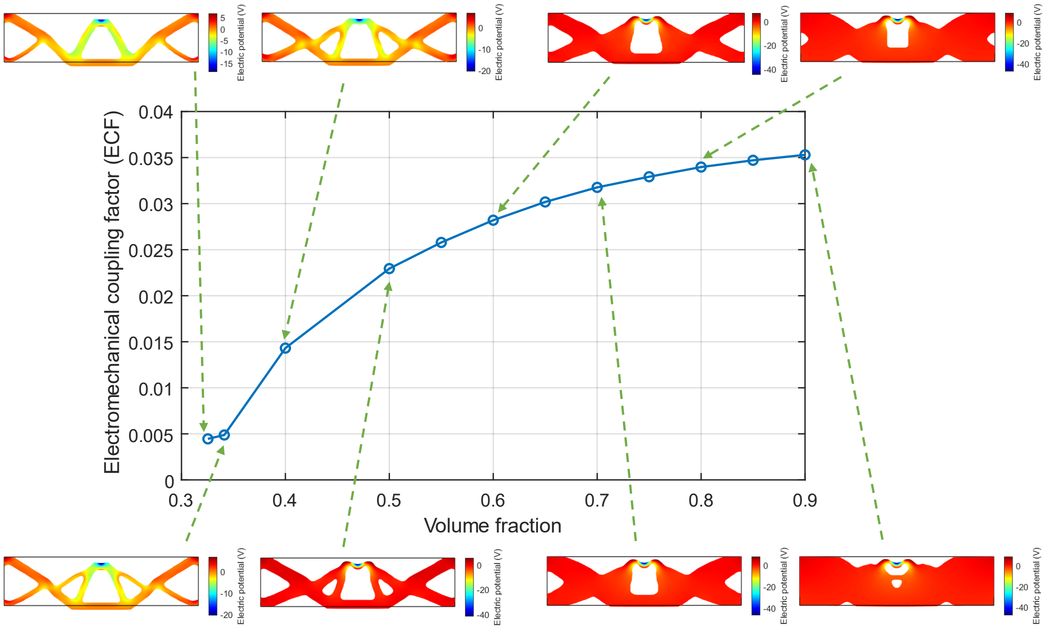

Figure 12: Electromechanical coupling factors for optimized structures of flexoelectric double-clamped beam with respect to the volume fraction, and the force $F_2 = -10\text{N}$

the forces F_3=-0.5 N, F_3=-1 N, F_3=-2 N and F_3=-2.5 N, respectively, compared to the reference design.

We notice that in some situations (Beam problem, Table 1, and truncated pyramid, Table 3), the gain increases then decreases in Table 1 and decreases in Table 3 as the magnitude of the force increases, while we observe an opposite trend for the double-clamped beam problem (Table 2). The origin of this trend is not easy to explain, as it involves a complex combination of boundary conditions, load and final topology and nonlinear material response. One interesting topic for future studies would be to optimize the gain in combination with the force amplitude, to possibly harvest higher amount of energy. Such study is out of the present work.

The distribution of electric potentials and deformed configuration for optimal structures of flexoelectric truncated pyramid achieved by different forces are presented in Fig.15. It is clear that localized large deformations occurring on the top

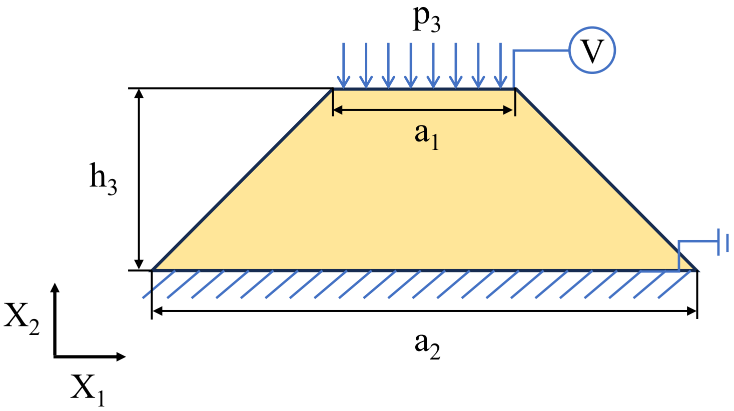

Figure 13: Compressed truncated pyramid-like soft dielectrics with open circuit boundary conditions: design domain

surface of the holes lead to a concentrated distribution of large electric potentials. An increase in the force applied during optimization will amplify the amplitude of the distributed electric potentials.

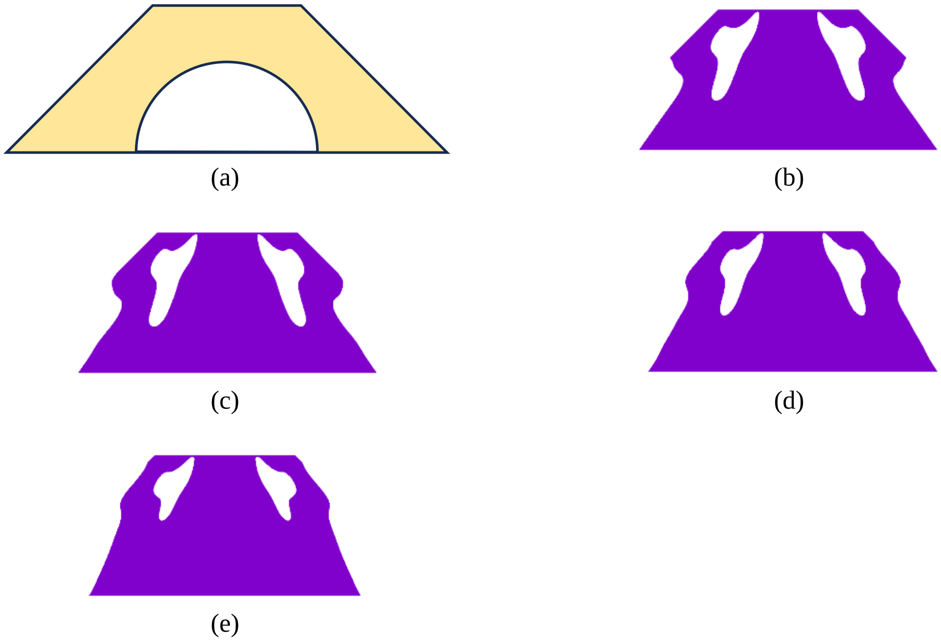

Figure 14: Reference structure and optimized designs for truncated pyramid obtained by different loads: (a) reference structure; (b) optimal design by load $p_3 = -0.5$N; (c) optimal design by load $p_3 = -1$N; (d) optimal design by load $p_3 = -2$N; (e) optimal design by load $p_3 = -2.5$N

Table 3: Electromechanical coupling factors (ECF) of optimal designs for flexoelectric truncated pyramid under different loads

Force	ECF (optimized)	ECF (reference)	Gain: $\mathrm{ECF}_{opt}/\mathrm{ECF}_{ref}$
-0.5 N	0.01877	2.5551×10^{-3}	7.3446
-1 N	0.01970	2.7881×10^{-3}	7.0646
-2 N	0.02108	3.4313×10^{-3}	6.1426
-2.5 N	0.02242	3.9178×10^{-3}	5.7234

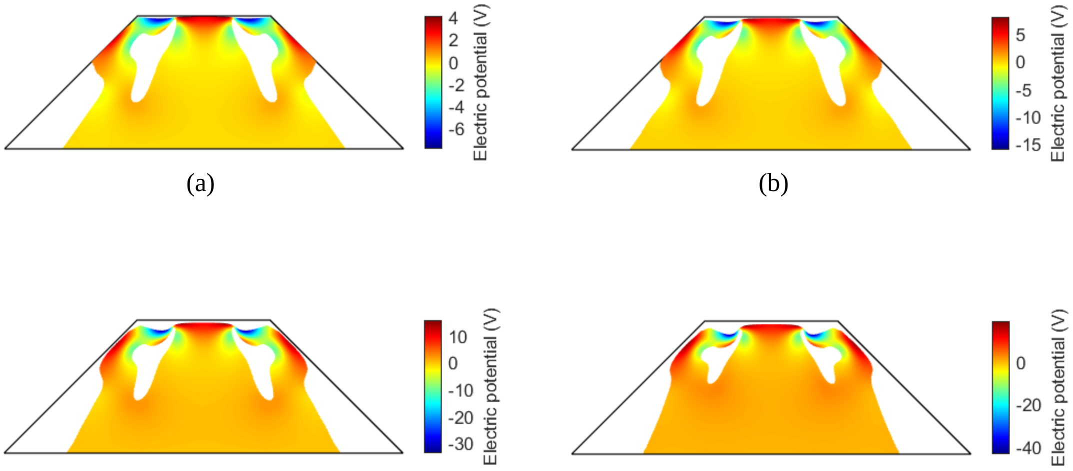

(a) (b) (c) (d)

Figure 15: Distribution of electric potentials and deformed configuration for optimal structures of truncated pyramid under different forces: (a) optimal design by pressure $p_3 = -0.5$N; (b) optimal design by pressure $p_3 = -1$N; (c) optimal design by pressure $p_3 = -2$N; (d) optimal design by pressure $p_3 = -2.5$N

8. Conclusion

In this study, a nonlinear topology optimization framework has been proposed for flexoelectric soft dielectrics subjected to large deformations. A numerical framework for finite-deformation nonlinear dielectrics was first derived, ensuring C^1-continuity for fourth-order flexoelectric partial differential equations using iso-geometric analysis (IGA). We have described the procedure for coherent linearizations and IGA discretizations. At the topology optimization stage, an innovative and efficient stress density function (SDF) interpolation scheme has been proposed. In this scheme, the electromechanical and hyperelastic SDFs were interpolated on the basis of the SIMP model, while a linear material interpolation model was used for the dielectric component.

Throughout our numerical analysis, we have demonstrated the good performance of the proposed stress density function (SDF) interpolation scheme in nonlinear electromechanical optimization scenarios. We have extended an energetic remedy scheme[71] for void regions, to the optimization of soft dielectrics, preventing distorting deformations in low stiffness elements. Furthermore, optimization based solely on the electromechanical coupling factor objective can lead to the formation of disconnected structures if mechanical stiffness considerations are not taken into account. To ensure the generation of physically acceptable optimal structures, we introduced a compliance constraint to regulate mechanical stiffness, thus preventing the appearance of disconnected domains.

The influence of large deformations on the optimization of flexible flexoelectric materials has been demonstrated, as well as their effects on the gains obtained. Size effects have also been shown in this context. The topology optimization framework we have proposed for nonlinear flexible flexoelectric materials takes full advantage of large deformations, resulting in a significant improvement in the electromechanical coupling factors in the optimized structures. The electromechanical coupling factors (ECF) of optimized structures in all the above cases show improvements of up to 9 times over those of reference designs. It has been shown that in some situations, non-linear effects, i.e. the magnitude of the prescribed load, can increase the gains in electromechanical coupling factors, while they can reduce them in other cases. Proposing a framework for generally improving ECFs as a function of applied forces is an interesting avenue to explore in future studies.

9. Acknowledgments

Xing Chen acknowledges the support from China Scholarship Council (CSC No. 202106370116)

References

[1] O. Auciello, D. M. Aslam, Review on advances in microcrystalline, nanocrystalline and ultrananocrystalline diamond films-based micro/nano-electromechanical systems technologies, Journal of Materials Science 56 (2021) 7171–7230.

[2] A. Erturk, D. J. Inman, Piezoelectric energy harvesting, John Wiley & Sons, 2011.

[3] N. Sezer, M. Koç, A comprehensive review on the state-of-the-art of piezoelectric energy harvesting, Nano Energy 80 (2021) 105567. `doi:https://doi.org/10.1016/j.nanoen.2020.105567`.

[4] W. R. Ali, M. Prasad, Piezoelectric mems based acoustic sensors: A review, Sensors and Actuators A: Physical 301 (2020) 111756. `doi:https://doi.org/10.1016/j.sna.2019.111756`.

[5] K. Uchino, Piezoelectric actuators 2006: expansion from it/robotics to ecological/energy applications, Journal of Electroceramics 20 (2008) 301–311.

[6] V. Mashkevich, K. Tolpygo, Electrical, optical and elastic properties of diamond type crystals, Soviet Physics JETP 5 (3) (Oct 1957).

[7] J. F. Scott, Lattice Perturbations in CaWO4 and CaMoO4, The Journal of Chemical Physics 48 (2) (1968) 874–876. `doi:10.1063/1.1668727`.

[8] A. G. Petrov, Flexoelectricity of model and living membranes, Biochimica et Biophysica Acta (BBA) - Biomembranes 1561 (1) (2002) 1–25. `doi:https://doi.org/10.1016/S0304-4157(01)00007-7`.

[9] A. G. Petrov, Electricity and mechanics of biomembrane systems: Flexoelectricity in living membranes, Analytica Chimica Acta 568 (1) (2006) 70–83, molecular Electronics and Analytical Chemistry. `doi:https://doi.org/10.1016/j.aca.2006.01.108`.

[10] Q. Deng, L. Liu, P. Sharma, Flexoelectricity in soft materials and biological membranes, Journal of the Mechanics and Physics of Solids 62 (2014) 209–227, sixtieth anniversary issue in honor of Professor Rodney Hill. `doi:https://doi.org/10.1016/j.jmps.2013.09.021`.

[11] F. Ahmadpoor, Q. Deng, L. P. Liu, P. Sharma, Apparent flexoelectricity in lipid bilayer membranes due to external charge and dipolar distributions, Phys. Rev. E 88 (2013) 050701. `doi:10.1103/PhysRevE.88.050701`.

[12] B. Chu, D. R. Salem, Flexoelectricity in several thermoplastic and thermosetting polymers, Applied Physics Letters 101 (10) (2012) 103905. `doi:10.1063/1.4750064`.

[13] X. Chen, X. Tang, X.-Z. Chen, Y.-L. Chen, X. Guo, H.-X. Ge, Q.-D. Shen, Nonvolatile data storage using mechanical force-induced polarization switching in ferroelectric polymer, Applied Physics Letters 106 (4) (2015) 042903. `doi:10.1063/1.4906859`.

[14] J. Liu, Y. Zhou, X. Hu, B. Chu, Flexoelectric effect in PVDF-based copolymers and terpolymers, Applied Physics Letters 112 (23) (2018) 232901. `doi:10.1063/1.5028344`.

[15] S. Kogan, Piezoelectric effect during inhomogeneous deformation and acoustic scattering of carriers in crystals, Soviet Physics-Solid State 5 (1964) 197 – 224.

[16] M. Čepič, B. c. v. Žekš, Flexoelectricity and piezoelectricity: The reason for the rich variety of phases in antiferroelectric smectic liquid crystals, Phys. Rev. Lett. 87 (2001) 085501. `doi:10.1103/PhysRevLett.87.085501`.

[17] P. V. Yudin, A. K. Tagantsev, Fundamentals of flexoelectricity in solids, Nanotechnology 24 (43) (2013). `doi:10.1088/0957-4484/24/43/432001`.

[18] P. Zubko, G. Catalan, A. Tagantsev, Flexoelectric effect in solids, Annual Review of Materials Research 43 (1) (2013) 387–421. `doi:10.1146/annurev-matsci-071312-121634`.

[19] B. Wang, Y. Gu, S. Zhang, L.-Q. Chen, Flexoelectricity in solids: Progress, challenges, and perspectives, Progress in Materials Science 106 (2019) 100570. `doi:https://doi.org/10.1016/j.pmatsci.2019.05.003`.

[20] R. Pelrine, R. Kornbluh, Q. Pei, J. Joseph, High-speed electrically actuated elastomers with strain greater than 100%, Science 287 (5454) (2000) 836–839.

[21] X. Zhao, Z. Suo, Theory of dielectric elastomers capable of giant deformation of actuation, Phys. Rev. Lett. 104 (2010) 178302. `doi:10.1103/PhysRevLett.104.178302`.

[22] U. Gupta, L. Qin, Y. Wang, H. Godaba, J. Zhu, Soft robots based on dielectric elastomer actuators: a review, Smart Materials and Structures 28 (10) (2019) 103002. `doi:10.1088/1361-665X/ab3a77`.

[23] J. Yvonnet, L. Liu, A numerical framework for modeling flexoelectricity and maxwell stress in soft dielectrics at finite strains, Computer Methods in Applied Mechanics and Engineering 313 (2017) 450 – 482. `doi:10.1016/j.cma.2016.09.007`.

[24] A. K. Tagantsev, Piezoelectricity and flexoelectricity in crystalline dielectrics, Phys. Rev. B 34 (1986) 5883–5889. `doi:10.1103/PhysRevB.34.5883`.

[25] R. Maranganti, N. D. Sharma, P. Sharma, Electromechanical coupling in nonpiezoelectric materials due to nanoscale nonlocal size effects: Green's function solutions and embedded inclusions, Phys. Rev. B 74 (2006) 014110. `doi:10.1103/PhysRevB.74.014110`.

[26] S. Shen, S. Hu, A theory of flexoelectricity with surface effect for elastic dielectrics, Journal of the Mechanics and Physics of Solids 58 (5) (2010) 665–677. `doi:https://doi.org/10.1016/j.jmps.2010.03.001`.

[27] L. Liu, An energy formulation of continuum magneto-electro-elasticity with applications, Journal of the Mechanics and Physics of Solids 63 (2014) 451–480. `doi:https://doi.org/10.1016/j.jmps.2013.08.001`.

[28] K. Wang, B. Wang, Non-linear flexoelectricity in energy harvesting, International Journal of Engineering Science 116 (2017) 88–103. `doi:https://doi.org/10.1016/j.ijengsci.2017.02.010`.
URL `https://www.sciencedirect.com/science/article/pii/S0020722516310436`

[29] M. Mojahedi, M. Rahaeifard, A size-dependent model for coupled 3d deformations of nonlinear microbridges, International Journal of Engineering Science 100 (2016) 171–182. `doi:https://doi.org/10.1016/j.ijengsci.2015.12.010`.

[30] K. Wang, T. Kitamura, B. Wang, Nonlinear pull-in instability and free vibration of micro/nanoscale plates with surface energy – a modified couple stress theory model, International Journal of Mechanical Sciences 99 (2015) 288–296. `doi:https://doi.org/10.1016/j.ijmecsci.2015.05.006`.

[31] A. Erturk, D. J. Inman, A Distributed Parameter Electromechanical Model for Cantilevered Piezoelectric Energy Harvesters, Journal of Vibration and Acoustics 130 (4) (2008) 041002. `doi:10.1115/1.2890402`.

[32] F. Cottone, H. Vocca, L. Gammaitoni, Nonlinear energy harvesting, Phys. Rev. Lett. 102 (2009) 080601. `doi:10.1103/PhysRevLett.102.080601`.

[33] N. Sharma, R. Maranganti, P. Sharma, On the possibility of piezoelectric nanocomposites without using piezoelectric materials, Journal of the Mechanics and Physics of Solids 55 (11) (2007) 2328–2350. `doi:https://doi.org/10.1016/j.jmps.2007.03.016`.

[34] A. Abdollahi, C. Peco, D. Millán, M. Arroyo, I. Arias, Computational evaluation of the flexoelectric effect in dielectric solids, Journal of Applied Physics 116 (9) (2014) 093502. `doi:10.1063/1.4893974`.

[35] A. Abdollahi, D. Millán, C. Peco, M. Arroyo, I. Arias, Revisiting pyramid compression to quantify flexoelectricity: A three-dimensional simulation study, Phys. Rev. B 91 (2015) 104103. `doi:10.1103/PhysRevB.91.104103`.

[36] S. Mao, P. Purohit, N. Aravas, Mixed finite-element formulations in piezoelectricity and flexoelectricity, Proceedings of the Royal Society A: Mathematical, Physical and Engineering Sciences 472 (2190) (2016) 20150879.

[37] B. Nguyen, X. Zhuang, T. Rabczuk, Numerical model for the characterization of maxwell-wagner relaxation in piezoelectric and flexoelectric composite material, Computers & Structures 208 (2018) 75–91. `doi:https://doi.org/10.1016/j.compstruc.2018.05.006`.

[38] D. Codony, O. Marco, S. Fernández-Méndez, I. Arias, An immersed boundary hierarchical b-spline method for flexoelectricity, Computer Methods in Applied Mechanics and Engineering 354 (2019) 750–782. `doi:https://doi.org/10.1016/j.cma.2019.05.036`.

[39] X. Chen, S. Yao, J. Yvonnet, Dynamic analysis of flexoelectric systems in the frequency domain with isogeometric analysis, Computational Mechanics 71 (2) (2023) 353–366.

[40] T. Thai, T. Rabczuk, X. Zhuang, A large deformation isogeometric approach for flexoelectricity and soft materials, Computer Methods in Applied Mechanics and Engineering 341 (2018) 718–739.

[41] T. Q. Thai, X. Zhuang, H. S. Park, T. Rabczuk, A staggered explicit-implicit isogeometric formulation for large deformation flexoelectricity, Engineering Analysis with Boundary Elements 122 (2021) 1–12. `doi:https://doi.org/10.1016/j.enganabound.2020.10.004`.

[42] D. Codony, P. Gupta, O. Marco, I. Arias, Modeling flexoelectricity in soft dielectrics at finite deformation, Journal of the Mechanics and Physics of Solids 146 (2021) 104182. `doi:https://doi.org/10.1016/j.jmps.2020.104182`.

[43] F. Deng, W. Yu, X. Liang, S. Shen, A mixed finite element method for large deformation of flexoelectric materials, Applied Mathematical Modelling 118 (2023) 303–321. `doi:https://doi.org/10.1016/j.apm.2023.01.029`.

[44] A. H. Rahmati, S. Yang, S. Bauer, P. Sharma, Nonlinear bending deformation of soft electrets and prospects for engineering flexoelectricity and transverse (d 31) piezoelectricity, Soft matter 15 (1) (2019) 127–148.

[45] J. Yvonnet, X. Chen, P. Sharma, Apparent flexoelectricity due to heterogeneous piezoelectricity, Journal of Applied Mechanics 87 (11) (2020) 111003.

[46] N. Mawassy, H. Reda, J.-F. Ganghoffer, V. A. Eremeyev, H. Lakiss, A variational approach of homogenization of piezoelectric composites towards piezoelectric and flexoelectric effective media, International Journal of Engineering Science 158 (2021) 103410. `doi:https://doi.org/10.1016/j.ijengsci.2020.103410`.

[47] N. Mawassy, H. Reda, J.-F. Ganghoffer, H. Lakiss, Control of the piezoelectric and flexoelectric homogenized properties of architected materials by tuning their inner topology, Mechanics Research Communications 127 (2023) 104034. `doi:https://doi.org/10.1016/j.mechrescom.2022.104034`.

[48] M. Nasimsobhan, J.-F. Ganghoffer, M. Shamshirsaz, Construction of piezoelectric and flexoelectric models of composites by asymptotic homogenization and application to laminates, Mathematics and Mechanics of Solids 27 (4) (2022) 602–637. `arXiv:https://doi.org/10.1177/10812865211030317`, `doi:10.1177/10812865211030317`.

[49] M. P. Bendsøe, O. Sigmund, Topology Optimization Theory, Methods, and Applications-second edition, 2013.

[50] M. P. Bendsøe, Optimal shape design as a material distribution problem, Structural optimization 1 (4) (1989) 193–202.

[51] G. I. Rozvany, M. Zhou, T. Birker, Generalized shape optimization without homogenization, Structural optimization 4 (3-4) (1992) 250–252.

[52] Y. Xie, G. Steven, A simple evolutionary procedure for structural optimization, Computers and Structures 49 (5) (1993) 885 – 896. `doi:10.1016/0045-7949(93)90035-C`.

[53] M. Y. Wang, X. Wang, D. Guo, A level set method for structural topology optimization, Computer Methods in Applied Mechanics and Engineering 192 (1) (2003) 227 – 246. `doi:/10.1016/S0045-7825(02)00559-5`.

[54] G. Allaire, F. Jouve, A.-M. Toader, Structural optimization using sensitivity analysis and a level-set method, Journal of computational physics 194 (1) (2004) 363–393.

[55] B. Bourdin, A. Chambolle, Design-dependent loads in topology optimization, ESAIM: Control, Optimisation and Calculus of Variations 9 (2003) 19–48.

[56] X. Guo, W. Zhang, W. Zhong, Doing Topology Optimization Explicitly and Geometrically—A New Moving Morphable Components Based Framework, Journal of Applied Mechanics 81 (8) (2014) 081009. `doi:10.1115/1.4027609`.

[57] W. Zhang, J. Chen, X. Zhu, J. Zhou, D. Xue, X. Lei, X. Guo, Explicit three dimensional topology optimization via moving morphable void (mmv) approach, Computer Methods in Applied Mechanics and Engineering 322 (2017) 590–614. `doi:https://doi.org/10.1016/j.cma.2017.05.002`.

[58] Z. Zhang, Y. Li, W. Zhou, X. Chen, W. Yao, Y. Zhao, Tonr: An exploration for a novel way combining neural network with topology optimization, Computer Methods in Applied Mechanics and Engineering 386 (2021) 114083. `doi:https://doi.org/10.1016/j.cma.2021.114083`.
URL `https://www.sciencedirect.com/science/article/pii/S004578252100414X`

[59] X. Chen, J. Yvonnet, S. Yao, H. Park, Topology optimization of flexoelectric composites using computational homogenization, Computer Methods in Applied Mechanics and Engineering 381 (2021) 113819. `doi:https://doi.org/10.1016/j.cma.2021.113819`.

[60] X. Chen, J. Yvonnet, H. Park, S. Yao, Enhanced converse flexoelectricity in piezoelectric composites by coupling topology optimization with homogenization, Journal of Applied Physics 129 (24) (2021) 245104. `doi:10.1063/5.0051062`.

[61] S. Nanthakumar, X. Zhuang, H. Park, T. Rabczuk, Topology optimization of flexoelectric structures, Journal of the Mechanics and Physics of Solids 105 (2017) 217 – 234. `doi:10.1016/j.jmps.2017.05.010`.

[62] H. Ghasemi, H. Park, T. Rabczukk, A level-set based iga formulation for topology optimization of flexoelectric materials, Computer Methods in Applied Mechanics and Engineering 313 (2017) 239 – 258. `doi:10.1016/j.cma.2016.09.029`.

[63] H. Ghasemi, H. S. Park, T. Rabczuk, A multi-material level set-based topology optimization of flexoelectric composites, Computer Methods in Applied Mechanics and Engineering 332 (2018) 47 – 62. `doi:10.1016/j.cma.2017.12.005`.

[64] J. López, N. Valizadeh, T. Rabczuk, An isogeometric phase–field based shape and topology optimization for flexoelectric structures, Computer Methods in Applied Mechanics and Engineering 391 (2022) 114564. `doi:https://doi.org/10.1016/j.cma.2021.114564`.

[65] W. Zhang, X. Yan, Y. Meng, C. Zhang, S.-K. Youn, X. Guo, Flexoelectric nanostructure design using explicit topology optimization, Computer Methods in Applied Mechanics and Engineering 394 (2022) 114943. `doi:https://doi.org/10.1016/j.cma.2022.114943`.

[66] X. Chen, S. Yao, J. Yvonnet, Multiscale topology optimization of an electromechanical dynamic energy harvester made of non-piezoelectric material, Structural and Multidisciplinary Optimization (2024).

[67] R. Ortigosa, J. Martínez-Frutos, A. Gil, A computational framework for topology optimisation of flexoelectricity at finite strains considering a multi-field micromorphic approach, Computer Methods in Applied Mechanics and Engineering 401 (2022) 115604. `doi:https://doi.org/10.1016/j.cma.2022.115604`.

[68] X. Zhuang, T. Q. Thai, T. Rabczuk, Topology optimization of nonlinear flexoelectric structures, Journal of the Mechanics and Physics of Solids 171 (2023) 105117. `doi:https://doi.org/10.1016/j.jmps.2022.105117`.

[69] T. Hughes, J. Cottrell, Y. Bazilevs, Isogeometric analysis: Cad, finite elements, nurbs, exact geometry and mesh refinement, Computer Methods in Applied Mechanics and Engineering 194 (39) (2005) 4135–4195. `doi:https://doi.org/10.1016/j.cma.2004.10.008`.

[70] J. A. Cottrell, T. J. Hughes, Y. Bazilevs, Isogeometric analysis: toward integration of CAD and FEA, John Wiley & Sons, 2009.

[71] F. Wang, B. S. Lazarov, O. Sigmund, J. S. Jensen, Interpolation scheme for fictitious domain techniques and topology optimization of finite strain elastic problems, Computer Methods in Applied Mechanics and Engineering 276 (2014) 453–472. `doi:https://doi.org/10.1016/j.cma.2014.03.021`.

[72] J. P. Jarić, D. Kuzmanović, Z. Golubović, On tensors of elasticity, Theoretical and Applied Mechanics 35 (1-3) (2008) 119–136.

[73] C. De Boor, C. De Boor, A practical guide to splines, Vol. 27, springer-verlag New York, 1978.

[74] F. Wang, B. S. Lazarov, O. Sigmund, On projection methods, convergence and robust formulations in topology optimization, Structural and multidisciplinary optimization 43 (2011) 767–784.

[75] J. Gao, L. Gao, Z. Luo, P. Li, Isogeometric topology optimization for continuum structures using density distribution function, International Journal for Numerical Methods in Engineering 119 (10) (2019) 991–1017. `doi:https://doi.org/10.1002/nme.6081`.

[76] W. Zhu, J. Fu, N. Li, L. Cross, Piezoelectric composite based on the enhanced flexoelectric effects, Applied physics letters 89 (19) (2006) 192904.